# SANDIA REPORT

SAND89—2345 • UC—904
Unlimited Release
Printed May 1990

# Solderability Testing of Kovar With 60Sn40Pb Solder and Organic Fluxes

Paul T. Vianco, F. Michael Hosking, Jerome A. Rejent

**Prepared by**
**Sandia National Laboratories**
**Albuquerque, New Mexico 87185 and Livermore, California 94550**
**for the United States Department of Energy**
**under Contract DE-AC04-76DP00789**

---

Issued by Sandia National Laboratories, operated for the United States Department of Energy by Sandia Corporation.



Available to DOE and DOE contractors from
Office of Scientific and Technical Information
PO Box 62
Oak Ridge, TN 37831

Prices available from (615) 576-8401, FTS 626-8401

Available to the public from
National Technical Information Service
US Department of Commerce
5285 Port Royal Rd
Springfield, VA 22161

NTIS price codes
Printed copy: A03
Microfiche copy: A01

SAND89–2345
Unlimited Release
Printed May 1990

SAND--89-2345

DE90 013643

# Solderability Testing of Kovar With 60Sn40Pb Solder and Organic Fluxes

Paul T. Vianco, F. Michael Hosking, and Jerome A. Rejent
Solid-State Component Processing Division
F. Michael Hosking and Jerome A. Rejent
Physical Metallurgy Division
Sandia National Laboratories
Albuquerque, NM 87185

## Abstract

The solderability of 60Sn40Pb solder on Kovar was examined as a function of surface-cleaning procedure, flux, and solder-bath temperature. Organic-acid fluxes were more effective at lowering the contact angle than was a mildly activated, rosin-based (RMA) flux on chemically etched Kovar. The contact angles were as low as $29° \pm 5°$ as compared to $61° \pm 11°$, respectively. Varying the solder temperature through the range of 215°C to 288°C caused an insignificant change in the contact angle for the RMA flux and a decrease of the contact angle for a candidate water-based, organic-acid flux. The dilution strength of the flux and the elapsed cleaning time significantly influenced the solder-flux interfacial tension, $\gamma_{LF}$. T-peel strengths of Kovar-60Sn40Pb-OFHC copper joints had a low correlation with the contact angle derived from the solderability experiments. The results of the solderability tests and the T-peel mechanical tests, and subsequent microanalysis of the as-soldered and T-peel samples revealed that the best results for the RMA flux were achieved by using an electropolishing procedure and a solder temperature of 240°C to 260°C. A relatively low contact angle of $31° \pm 2°$ was observed, with no evidence of cracking or thick-film intermetallic formation at the Kovar-solder interface. T-peel strengths were nominally $9.4° \pm 0.5 \times 10^6$ dyn/cm.

# Acknowledgments

The authors thank the following individuals whose talents contributed to this report: Mark McAllaster (1822) who fabricated the metallographic samples; R. Ellen Semerge (formerly with 1822) for the x-ray microprobe analysis; David Huskisson (1822) and Fred Greulich (1822), who performed the scanning electron microscopy; and Joseph Dal Porto (7413) and Charles Robino (1831) for their thoughtful review of this report.

# Contents

## Figures

## Figures (continued)



## Table

# Solderability Testing of Kovar With 60Sn40Pb Solder and Organic Fluxes

## Introduction

### 1.1 Mercury Switch #371925—Tinning of the Kovar Lead Wires

The application of mercury switch #371925 required its installation on a circuit board by soldering with 60Sn40Pb alloy. Pretinning of the Kovar leads emanating from the switch body by immersion in the liquid 60Sn40Pb alloy was intended to assist in attaching the switch to the circuit board. The rosin-based, mildly activated flux Alpha$^{TM}$ 611 was applied to the leads before the pretinning process.

During pretinning, however, poor wetting of the Kovar leads by the solder was observed. In locations where wetting appeared successful, closer observations showed significant *dewetting* . The primary goal of the study described in this report was to determine changes to the process that would improve the wetting of the Kovar leads by the 60Sn40Pb solder.

The process parameters examined in this investigation were: (1) the type and concentration of flux used on the leads before pretinning; (2) the cleaning procedures to which the leads were exposed before fluxing and pretinning; and (3) the operating parameters of the solder bath, such as temperature.

Kovar coupons 2.54 × 2.54 × 0.028 cm were evaluated for wetting. These coupons were exposed to the same treatment as that received by the Kovar leads during fabrication of the mercury switch.

### 1.2 Quantitative Analysis of Solderability

The term "solderability" refers to the tendency of a solder alloy to wet the substrate surface. As Figure 1 shows, the equilibrium configuration of the liquid metal on a substrate surface covered with flux is determined by the force balance between the horizontal components of the three interfacial tensions, as described by Young's equation:

$$\gamma_{SF} - \gamma_{SL} = \gamma_{LF} \cos \theta_c \ , \qquad (1)$$

where

$\gamma_{SF}$ = the solid-flux interfacial tension
$\gamma_{SL}$ = the solid-liquid (solder) interfacial tension
$\gamma_{LF}$ = the liquid (solder)-flux interfacial tension
$\theta_c$ = the contact angle.

The wetting ability of the liquid *increases* as the contact angle *decreases*. Therefore, the value of $\theta_c$ serves as a criterion that quantitatively describes solderability by taking into account the effects of all the interfacial tensions.

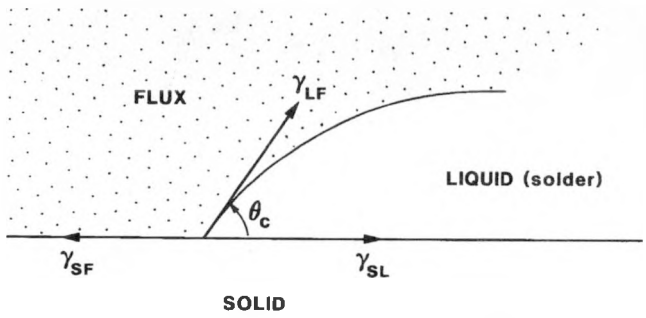


**Figure 1.** Equilibrium configuration between the interfacial tensions of the sessile drop configuration.

Several experimental techniques have been devised to measure the contact angle of a molten solder (or for that matter, any liquid) resting on a solid surface. Such methods include direct observations of the angle or photographs of the drop from which the contact angle can be obtained from calculations based on the drop's geometry[1]. However, the method developed by Wilhelmy[2] and used in this investigation to determine $\theta_c$ and is similar in principle to the rise of a liquid inside a capillary tube.[1] To begin with, a sheet of the base material is vertically immersed into the liquid solder (Figure 2a). The solder rises up the coupon's surface to a final height, as determined by

the equilibrium described by Young's equation (Figure 2b). From the geometry of the meniscus and the material properties of the solder, we can then calculate the contact angle. The procedures to make these calculations are described next.

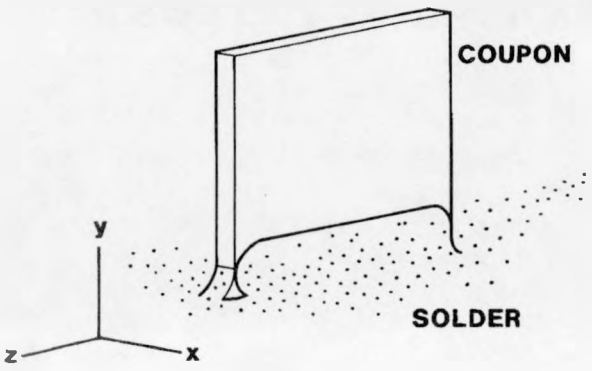


(a)

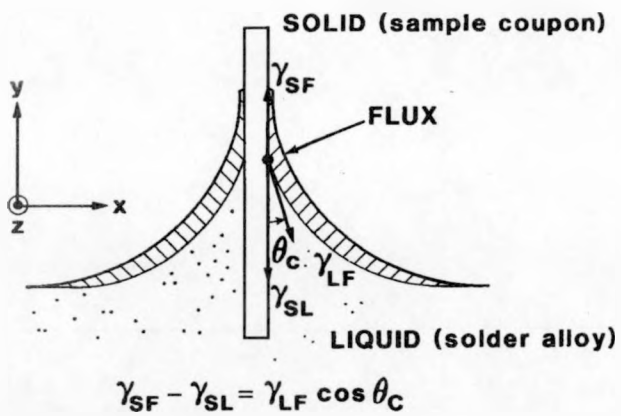


(b)

**Figure 2.** Solderability evaluation. (a) Testing geometry (b) The equilibrium balance of interfacial tensions as described by Young's equation for the solderability test.

The determination of $\theta_c$ from the vertically immersed coupon is based on: (1) the profile of the meniscus surface, and (2) the mass of solder contained in the meniscus.[3,4] As the schematic of the meniscus profile in Figure 3 shows, a force balance exists in the vertical direction between the weight of the solder in the differential volume ydx (assuming unit thickness) and the net upward force provided by the surface tension:

$$\gamma_{LF}\sin(\phi+d\phi)-\gamma_{LF}\sin\phi-\rho g y\, dx = 0, \qquad (2)$$

where g is the acceleration due to gravity and $\rho$ is the density of the solder. Through a series of algebraic manipulations detailed in Reference 5, an equation is obtained that describes the profile of the meniscus surface in which the dependent variable $\theta$ can be calculated as a function of the distance, y:

$$1 - \sin\theta = \frac{\rho g y^2}{2\gamma_{LF}} . \qquad (3)$$

At the coupon surface, y=H and $\theta=\theta_c$; $\theta_c$is the contact angle. Equation (3) becomes:

$$1 - \sin\theta_c = \frac{\rho g H^2}{2\gamma_{LF}} . \qquad (4)$$

Therefore, $\theta_c$ can be determined if H and $\gamma_{LF}$ are known. H is an experimentally measured parameter. To obtain $\gamma_{LF}$, requires measuring the second property of the meniscus, its weight.

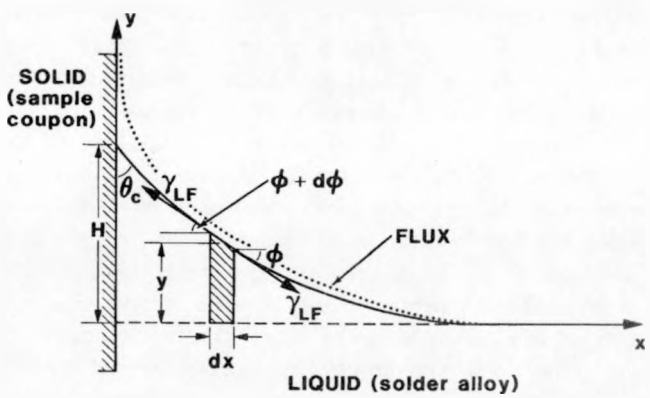


- $\theta = 90° - \phi$
- $\theta_c$ = THE CONTACT ANGLE
- H = THE MENISCUS HEIGHT

**Figure 3.** Geometric properties of the meniscus used to calculate the weight of risen solder. $\gamma_{LF}$ is the liquid solder-flux interfacial tension. Typical values of H are 1 to 3 mm.

Assuming that the meniscus profile is uniform around the coupon perimeter, we find that the weight of the solder in the meniscus, W, is simply the product:

$$W = \rho g P A , \qquad (5)$$

where P is the perimeter of the coupon and A is the cross-sectional area of the meniscus profile. The expression for A (the detailed calculation is located in

Appendix A) is given as:

$$A = \frac{H}{2}\sqrt{\frac{4\gamma_{LF}}{\rho g} - H^2} \ . \tag{6}$$

The weight of the meniscus is also an experimentally measured parameter. Therefore, solving for A in Eq (5), and the expression for A into Eq (6) results in an expression for $\gamma_{LF}$:

$$\gamma_{LF} = \frac{\rho g}{4}\left[\frac{4W^2}{(\rho g P H)^2} + H^2\right] . \tag{7}$$

Incorporating this equation into Eq (4) results in this expression for the contact angle, $\theta_c$:

$$\theta_C = \arcsin\left[\frac{4W^2 - (\rho g P H^2)^2}{4W^2 + (\rho g P H^2)^2}\right] . \tag{8}$$

Although the derivation leading to Eqs (7) and (8) is based in principle on References 4 and 5, we used the explicit expression for W derived from the equation for the meniscus cross section, Eq (6), which was not done in those citations.

The values of $\gamma_{LF}$ and $\theta_c$ resulting from the use of Eqs (7) and (8) will differ from those calculated with the equations derived in Reference 5. The term, $\rho$, representing the solder density, has replaced the expression, $(\rho - \rho_o)$, used in Reference 5. The parameter, $\rho_o$, is the density of the flux. The term $(\rho - \rho_o)$ originates from a suspected buoyancy effect caused by the flux film overlaying the solder as it is displaced by the wetting solder. We question the existence of such a buoyancy effect since the flux merely rests over a small area of the solder surface; the solder is hardly *immersed* in a volume of flux. Because $\rho_o$can be as much as 12% of the value of $\rho$, its presence can overestimate $\gamma_{LF}$ by ~4%. The value of the contact angle is overestimated by ~17%.

In spite of the fundamental soundness of the derivation leading to Eqs (7) and (8), experimental observations clearly indicated the need for an empirical correction to the buoyancy force on the coupon. The apparent meniscus weight obtained from the wetting balance must not only be corrected for the buoyancy force caused by the immersion of the sample, but must also be adjusted for the additional buoyancy force created by the risen meniscus. The additional buoyancy term was calculated from an additional immersion "depth" of $(H\text{-}V_o)$ (Figure 4). The value of $V_o$ was obtained as follows: For a representative sample coupon from each experimental group, the quantity, $V_o$, was measured at each of the four corners by using a traveling-stage microscope. The average value of the four measurements, $V_o$, was then subtracted from the meniscus height, H, so that the difference, $(H\text{-}V_o)$, becomes the additional immersion depth of the coupon as a result of the meniscus rise. This number was added to the nominal immersion depth, (ID) of the coupon. The total buoyancy force then becomes:

$$BF = \rho \times g \times [(H - V_o) + (ID)] \times w \times t \ , \tag{9}$$

where w is the coupon width and t is the coupon thickness.

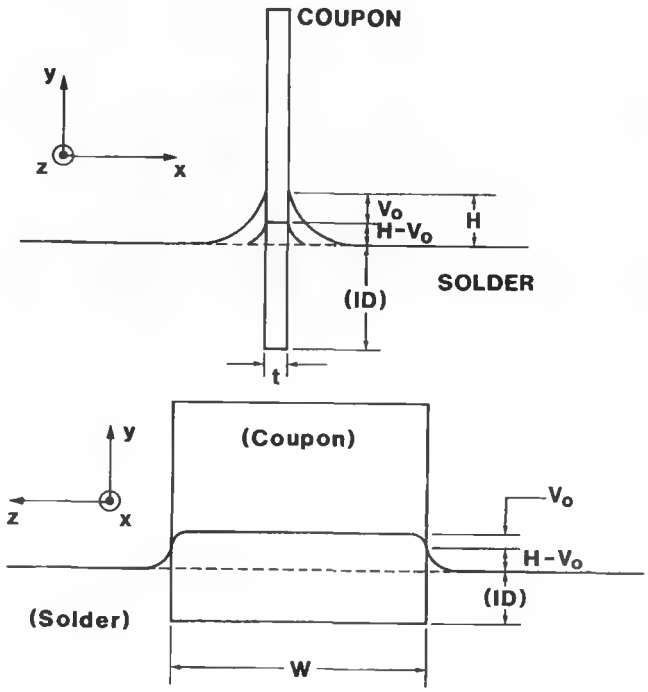


**Figure 4.** Meniscus geometry that describes the buoyancy force correction.

The experimental observations shown in Figure 4 indicate that the meniscus rise was not uniform around the sample perimeter. The lower meniscus height at the coupon corners is due to the absence of sufficient sample surface area to support the additional meniscus that must form around the sample's corner. Therefore, since the smaller weight generated by the reduced meniscus rise at the corners was compensated by the additional meniscus formed radially about each corner, we assumed that the total meniscus weight was equivalent to that resulting from a uniform meniscus rise about the entire sample perimeter.

## 1.3 T-Peel Mechanical Testing

To complement the solderability studies for which the theory was outlined above, we performed mechanical pull tests on joints formed between the Kovar coupon and copper. These tests were to determine (1) whether differences in mechanical strength behavior are attributable to the use of the different fluxes, and (2) how well the mechanical pull tests correlate with the solderability results such as the contact angle.

Mechanical strength was determined by the T-peel test (ASTM D-1876). The test samples consisted of two pieces of material bent into the form of an "L" and then bonded as shown in Figure 5a. The two free legs were then attached to the testing fixture and pulled apart. A schematic of the customary force-displacement curve is shown in Figure 5b. The peel force, F, is taken as the average value of the force after the initial spike; the peel strength is defined as F/L.

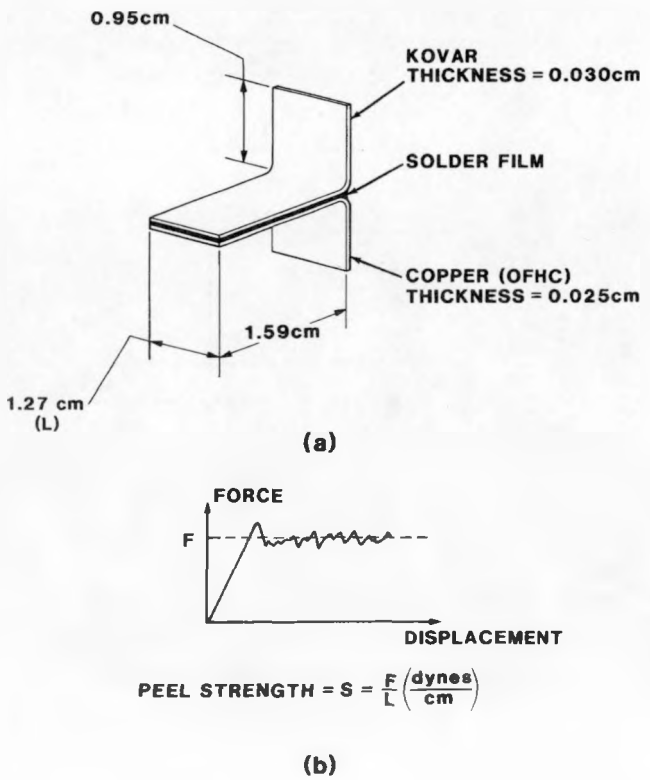


**Figure 5.** T-peel test (a) Schematic of the specimen (b) Force-displacement curve.

Although the accuracy of the T-peel test is limited by additional processes (such as deformation of the copper and Kovar sheets) occurring as the solder layer is pulled apart, other attributes must also be considered. First, the T-peel test allows for the same Kovar coupons and cleaning procedures as used in the solderability tests. Second, this sample geometry permits quick assembly of a large number of test samples for improved statistical accountability of the results. As in other mechanical tests, qualitative analysis of the fracture surface can provide valuable data as to where failure of the joint occurred (bulk solder, solder-base metal interface, or the base metal proper) and the mode of failure (ductile versus brittle, for example).

In the tests in this study, the pull samples were made of two materials; one "L" piece of Kovar and the other piece of copper, an arrangement selected to simulate a Kovar-copper bond. The Kovar piece was coated with the particular flux being tested; the copper sheet was fluxed with the rosin-based flux in all cases.

# 2. Experiment

## 2.1 Kovar Coupons

Sample coupons 0.028 × 2.54 × 2.54 cm were formed from sheets of Kovar (29Ni-17Co-0.2Mn-bal.Fe, nominal weight percents) and made available through Allied Signal/Kansas City Division. The coupons were then transferred to Fifth Dimension Inc., makers of the switch, and there exposed to exactly the same process conditions as experienced by the switch leads. A general description of the steps in this process follows:*

1. Chemical polish and etch
2. Exposure to high temperatures (oxidation) during the glass sealing process
3. Oxide removal by a second chemical etch

In addition to the plain Kovar specimens, testing was also performed on coupons electroplated with (1) 2.43 to 6.00 $\mu$m of nickel over the coupon, and (2), a second set of nickel-plated samples subsequently electroplated with 0.50 $\mu$m of gold. The nickel- and gold-nickel-plated layers, frequently used to improve the wetting of the Kovar surface, were included in this investigation for comparison. Processing of this particular component did not permit a plating option. Although the gold plating appeared to completely cover the Kovar surface, the nickel-plated samples were found to have a nonuniform coating; resulting in small exposed patches of the coupon. Observations presented later in this report show the consequences

*Disclosure of the details of these procedures is prohibited by their proprietary status.

of incomplete nickel plating on the wetting by the solder.

## 2.2 Solder Alloy

The solder alloy used in this study was 60Sn40Pb (wt.%) provided by Alpha™ Vaculloy and designated as 60SnBS. The alloy ingots were cut into small pieces, degreased, and then placed into AISI type 304 stainless steel cups that fit into both the meniscometer and wetting balance heating cavities. The cup diameter was sufficiently large to eliminate interactions between the coupon meniscus and the wall of the cup. The solder pots were constantly replenished with fresh solder to maintain the fluid level. After ~60 samples, we completely replaced the solder volumes in both the meniscometer and the wetting balance to remove the accumulated flux residues and residual metal contaminants (Au, Ni, and Fe) dissolved from the coupons by reactions with tin.

Solder for the T-peel tests came from Allied Semialloys in the form of a roll of strip 2.54 cm wide and 0.254 cm thick.

## 2.3 Evaluated Fluxes

In this study, we examined five fluxes:

1. Alpha™611
2. Alpha™250HF
3. Alpha™260HF
4. Blackstone™1452
5. Blackstone™2508

In this report, we refer to the fluxes as A611, A250HF, A260HF, B1452, and B2508, respectively. The A611 flux was the one originally designated for use in the pretinning of the Kovar leads. The remaining four fluxes, all water-soluble, halide-free, organic-acid liquids, were to be examined as possible replacements for the rosin-based A611. Because the halide ions—which are potentially corrosive to Kovar—were limited in these fluxes, they became viable alternatives for soldering electronic components. Table 1 gives some properties of the fluxes. Except where noted, each flux was diluted 1:1 by volume with isopropyl alcohol. Because the volume of each flux solution equaled the sum of the volume of flux and that of the alcohol, the density of the dilution was determined by the mixing rule. In all cases, the flux solutions were applied while they were at room temperature.

## 2.4 Cleaning Procedures

Wetting by the solder alloy is extremely sensitive to the surface conditions of the substrate (Kovar) material. Therefore, great care was taken to follow precisely the procedures for the handling and cleaning of not only the Kovar coupons but also the glassware and utensils used in the process. Because of the importance of these procedures, we furnish a detailed outline for them in this section.

***2.4.1 Procedure for Cleaning Glassware and Utensils***—All glassware used for the cleaning and storage of the sample coupons and of the handling instruments was first cleaned according to the following procedure:

1. Wash in solution of dish detergent and deionized water.
2. Rinse in deionized water.
3. Dry with $N_2$ gas.
4. Rinse in trichloroethylene.
5. Dry with $N_2$ gas.
6. Rinse in isopropyl alcohol.
7. Dry with $N_2$ gas.

The glassware was recleaned after ~60 samples were processed.

**Table 1. Properties of the fluxes**

| FLUX | DENSITY (20°C) g/cm[3] | pH[1](20°C) | RECOMMENDED OPERATING TEMPERATURE[2] °C | DESCRIPTION |
|---|---|---|---|---|
| ALPHA™ 611 | 0.877 | 4.9[2] | ~200° | ROSIN-BASED, MILDLY ACTIVATED<br>CORROSIVE: ABEITIC ACID<br>ACTIVATOR: AMINE HYDROBROMIDE<br>SOLVENT: ISOPROPYL ALCOHOL |
| BLACKSTONE™ 2508 | 1.080 | 3.4 | ~260° (<300°) | ORGANIC ACID<br>CORROSIVE: GLYCOLIC ACID<br>SOLVENT: WATER |
| BLACKSTONE™ 1452 | 1.254 | 2.7 | ~260° (<300°) | ORGANIC ACID<br>CORROSIVE: GLYCOLIC ACID<br>SOLVENT: WATER |
| ALPHA™ 260HF | 0.917 | 3.3[3] | >200° | ORGANIC ACID<br>CORROSIVE: GLYCOLIC ACID + ?<br>SOLVENT: ISOPROPYL ALCOHOL |
| ALPHA™ 250HF | 0.887 | 3.0[3] | ~200° | ORGANIC ACID<br>CORROSIVE: GLYCOLIC ACID AND ETHYL ESTERHYDROXYACETIC ACID<br>SOLVENT: ISOPROPYL ALCOHOL |

(1) MEASURED IN DEP'T 1820, SNL
(2) PRIVATE COMMUNICATION WITH MANUFACTURER
(3) 5% SOLUTION IN WATER

### *2.4.2 Procedure for Surface-Etching the Plain Kovar Coupons*

***Diversey 9-333 Surface Etch***—The as-received Kovar coupons were etched in Diversey 9-333 solution to remove the oxide from the specimen surface. A micrograph of the Kovar surface following the Diversey treatment is shown in Figure 6. An attack on the grain and twin boundaries is evident. Because the Diversey consists of a mixture of nitric, hydrochloric, and phosphoric acids as well as surfacting agents, the remaining steps of this procedure were designed to remove these residues, in particular the chloride ions resulting from the Kovar's sensitivity to corrosion by these species. The steps making up the Diversey surface-etch procedure as implemented by the switch manufacturer are outlined below:

1. Immerse 2 min in 300 mL of Diversey 9-333 held at 80°C to 85°C and agitated. Two batches of 5 coupons each per a 300-mL volume of Diversey.
2. Immerse 4 min in 300 mL of agitated hot tap water. Repeat 2 times with fresh volume of water.
3. Immerse 75 sec in 200 mL of agitated Dynadet solution.
4. Repeat step 2.
5. Immerse 75 sec in 200 mL of agitated deionized water. Repeat 2 times with fresh volume of water.
6. Immerse 75 sec in 200 mL of agitated acetone. Repeat 2 times with fresh volume of acetone.
7. Dry with $N_2$ gas.

The coupon-cleaning logistics are now briefly described. Each solderability test used 10 coupons; 4 of the coupons for meniscometer testing and the remaining 6 with the wetting balance. However, only 5 specimens were cleaned (and subsequently tested) at a time to minimize the differences in the time interval between the cleaning and fluxing steps as well as between the fluxing and testing steps for each of the coupons. For the first two batches of samples, precise time logs were kept to determine how long the cleaning process actually took. The average value was 36 min, 22 sec; the theoretical value was 34 min, 45 sec.

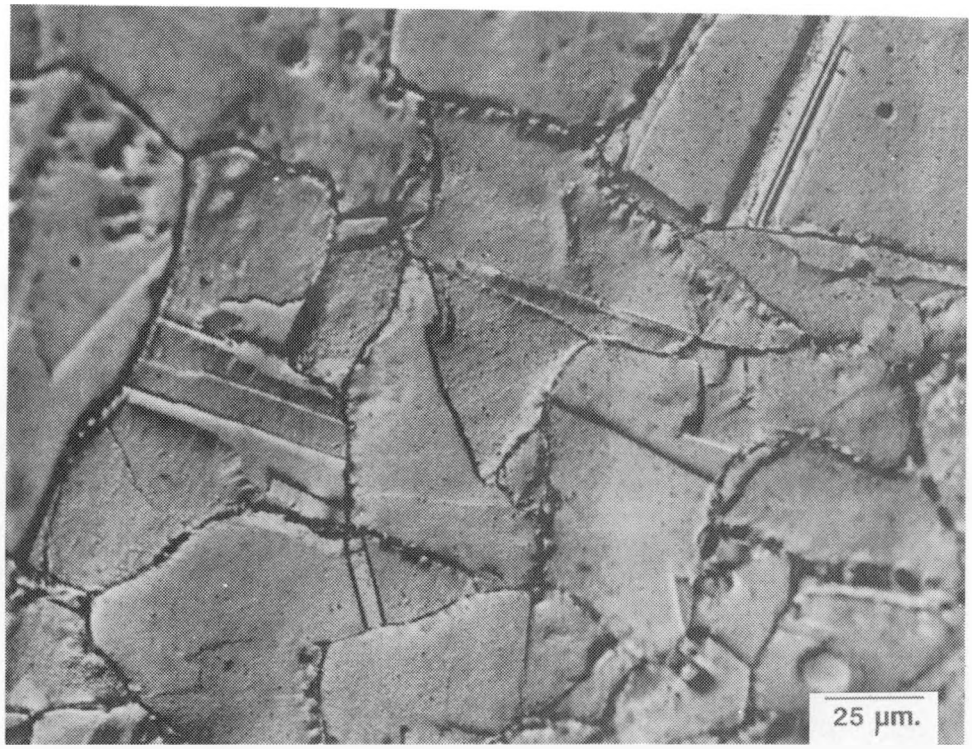


**Figure 6.** Optical micrograph (differential interference contrast) of the plain Kovar surface after the 2-min Diversey 9-333 etching procedure at 80°C to 85°C.

The samples were fluxed immediately after cleaning to limit exposure of the fresh surface to atmosphere, with time records maintained on each coupon in the batch. The samples were identified by the sequence in which each was fluxed (first, second, . . . fifth). The coupons were fluxed one at a time by immersing them ~1.2 cm into the particular flux-alcohol dilution for 5 sec, after which they were suspended on a wire to dry. After the fifth coupon had been fluxed, 10 min were allowed to elapse before performing the meniscometer or wetting balance tests. The coupons were chosen for testing in the same order in which they were fluxed.

Finally, we took care to visually observe the solvents and chemicals used for cleaning paying particular attention to residues and discoloration of the materials. For example, a batch of Diversey solution appeared "cloudy" as compared to earlier supplies. This change in transparency was due to an absence of wetting agents in the solution; a fact that was substantiated when a control group of coupons showed unexpectedly poor solderability.

***Electropolishing***—Figure 7 is a schematic of the equipment used to electrolytically polish the Kovar coupons. The electrolyte selected for this procedure contained 9 parts of acetic acid and 1 part of perchloric acid (60%)[5] for a total volume of 250 mL. Each volume of 250 mL was used to clean 5 coupons. The cathode was made of AISI type 347 stainless steel screen. The cooling bath maintained the electrolyte at an operating temperature of 30°C. To determine the voltage-current parameters necessary for optimizing the polishing process, we obtained the electropolishing curve under voltage control for an as-received Kovar sample (Figure 8). Note a small polishing plateau at ~10 V (0.5 A). Although a stable polishing film developed on the sample surface (brown-red indicating the presence of iron ions[6]) without gas evolution, the surface polished rather slowly. To increase the effectiveness of the process, we raised the voltage to 20 V. The corresponding current was 1.5 A, giving rise to a current density of 0.124 A/cm$^2$. In spite of some gas evolution, an excellent surface was obtained after 5 min. An example is shown in Figure 9. We observed the presence of some second-phase particles and a very slight etching of twin boundaries. A slight agitation to the bath was provided by a magnetic stirrer. For subsequent sample preparation, the electrolytic cell was operated under *current* control so that a constant and reproducible polishing action could be maintained as the ion loading of the electrolyte changed with time of use.

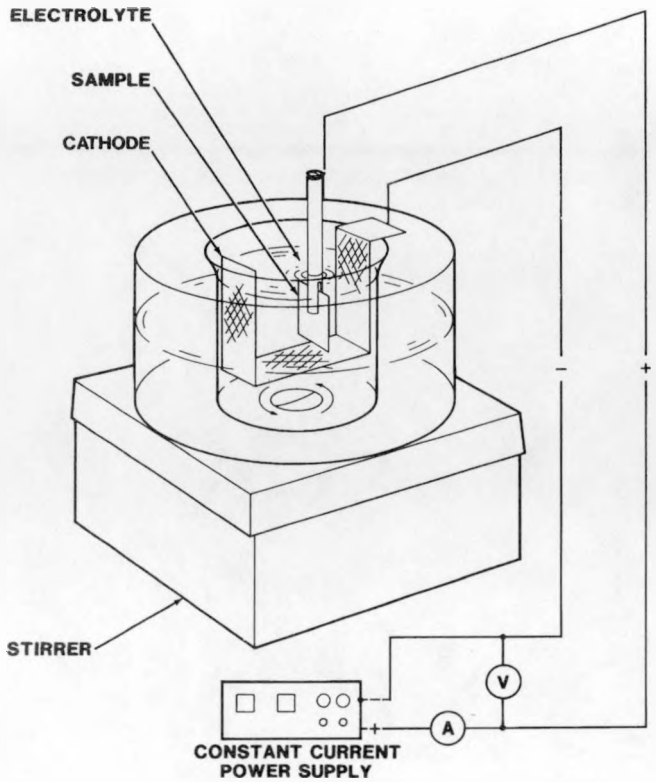


**Figure 7.** Schematic of the electrolytic polishing apparatus. The sample is 2.54 *cm* square; all other features have been similarly scaled in the drawing.

A detailed description of the electropolishing procedure follows. (One sample at a time was loaded into a specially designed holder made of AISI type 304 stainless steel.)

1. Sample was lowered into the electrolyte and the current established at 1.5 A. The polishing time was 5 min.
2. Sample was removed from the electrolyte, rinsed with a jet of deionized water to wash away all traces of the polishing film, and then suspended in a beaker of deionized water until five samples had been polished.

The elapsed time to complete five coupons was ~36 min (the theoretical value was 30 min). The material lost in the electropolishing process resulted in a reduction of the thickness dimension of ~0.0003 in. as compared to the Diversey-cleaned coupons. No other dimensional changes to the samples were observed between the two cleaning procedures. At this point, some groups of samples were processed through the Diversey surface etch treatment, as described in Section 2.4.2. Otherwise, the coupons were further processed by the following steps to thoroughly remove any residues from the electrolyte (and to accommodate the manufacturer's capabilities):

1. Rinse 5 min in 250 mL of deionized water.
2. Immerse 2 min in 250 mL of Dynadet solution.
3. Immerse 2 min in 300 mL of agitated hot tap water. Repeat with a fresh volume of water.
4. Immerse 2 min in 250 mL of agitated deionized water. Repeat with a fresh volume of water.
5. Rinse 2 min in 250 mL of agitated acetone. Repeat with a fresh volume of acetone.
6. Dry with $N_2$ gas.

No difference in the solderability results beyond experimental variations was noted when the Diversey treatment was dropped from the electropolishing procedure. Following the electropolishing process, the samples were fluxed and tested according to the sequence of steps described earlier.

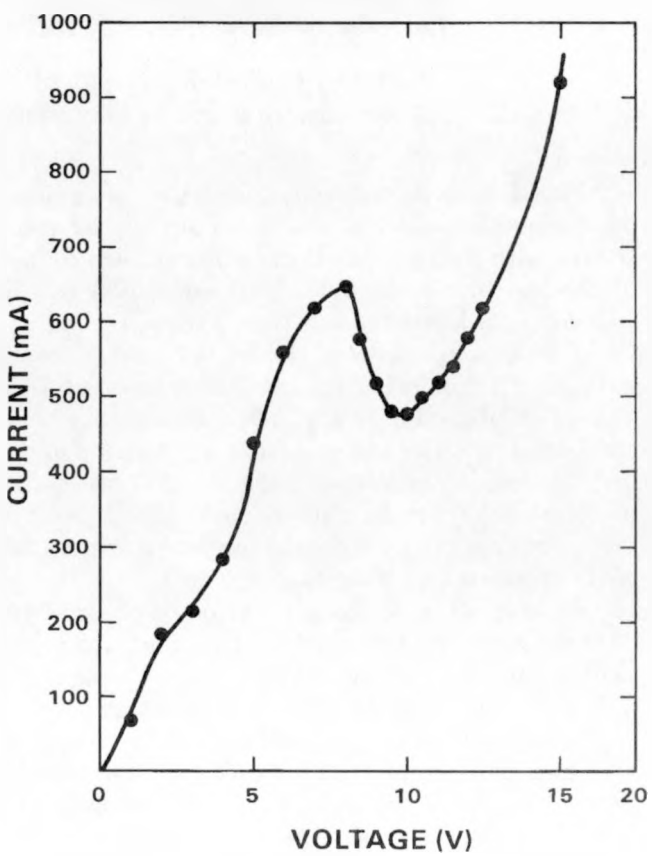


**Figure 8.** Static current-voltage curve for the electropolishing of the plain Kovar coupon in 250 mL of 9 parts acetic acid to 1 part perchloric acid (60%).

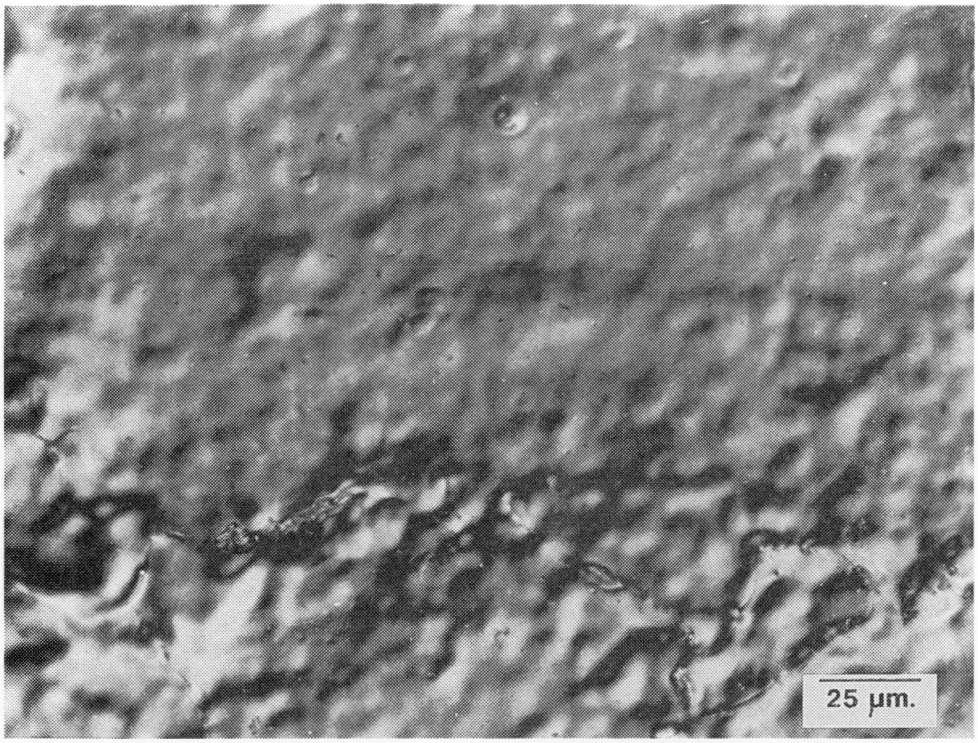


**Figure 9.** Optical micrograph (differential interference contrast) of the plain Kovar surface after the 5-min electropolishing treatment at 0.124 A/cm$^2$.

***2.4.3 Procedure for Cleaning Gold-Nickel-Plated and Gold-Plated Kovar***—The nickel- and gold-nickel-plated coupons were cleaned (degreased) as follows:

1. Immerse 3 min in agitated trichloroethylene.
2. Immerse 3 min in agitated isopropyl alcohol and repeat with a fresh volume of alcohol.
3. Dry with $N_2$ gas.

The fluxing and testing procedures were carried out immediately after surface cleaning and followed the steps outlined in Section 2.4.2.

***2.4.4 Procedure for Cleaning the T-Peel Test Components***—For this series of tests, three components had to be cleaned: the Kovar coupon, the 60Sn40Pb solder strip, and the copper sheet. The solder alloy, taken from a roll of strip, was cut into five pieces, each measuring 0.025 × 1.27 × 1.59 cm, and degreased by the following schedule (defined at SNL):

1. Ultrasonic cleaning for 1 min in trichloroethylene.
2. Ultrasonic rinsing for 1 min in isopropyl alcohol.
3. Dry in $N_2$ gas.

The solder "preforms" were stored in a glass-covered dish. Next, five sheets of oxygen-free, high-conductivity (OFHC) copper measuring 0.025 × 3.65 × 3.65 cm were cleaned as follows:

1. Immerse 2 min in agitated trichloroethylene.
2. Immerse 15 sec in HCl diluted 1:1 by volume with deionized water.
3. Rinse for 15 sec in agitated deionized water.
4. Immerse 3 min in agitated trichloroethylene.
5. Immerse 2 min in agitated isopropyl alcohol, and repeat with a fresh volume of alcohol.
6. Dry with $N_2$ gas.

The samples were immediately fluxed with Alpha$^{TM}$611 diluted 1:1 by volume with isopropyl alcohol and permitted to rest on a horizontal surface. The copper samples were processed *before* the Kovar so that the cleaning sequence and time intervals between fluxing and testing of the Kovar would more closely match those of the solderability-test coupons. Finally, the plain Kovar samples were cleaned according to one of the procedures described in Section 2.4.2. There were five samples to a batch. The gold-nickel specimens likewise were cleaned by the schedule in Section 2.4.3. Prior to cleaning, however, the Kovar samples were bent into an "L-shape" configuration, the long leg measuring 1.59 cm and the shorter

leg, 0.95 cm. For the plain Kovar specimens cleaned by means of the electropolishing treatment, the coupons were bent after cleaning. Following the surface treatment, the longer leg of each sample was immediately immersed for 5 sec in the particular flux to be evaluated. After the fifth (and final) sample of the batch had been fluxed, a 10-min period was allowed to elapse before assembling the complete T-peel pull sample.

***2.4.5 Flux Cleaning Procedures***—To make optical and scanning electron micrographs of the solder-coupon surface interface, we had to remove the flux residues from the specimen surfaces. It was imperative to perform this cleaning step as soon as possible after soldering because otherwise it was impossible to completely remove the charring deposits of the organic acid fluxes and the rosin flux residues.

For the rosin-based flux, A611, we chose the following cleaning steps:

1. Clean ultrasonically for 10 min in trichloroethylene.
2. Immerse 3 min in agitated isopropyl alcohol.
3. Immerse 3 min in agitated hot tap water.
4. Immerse 3 min in deionized water.
5. Immerse 75 sec in acetone.
6. Dry in $N_2$ gas.

Steps 1 and 2 removed the organic rosin base; the remaining steps rinsed away the activator.[7] Because the cleaning sequence could not be performed during the solderability tests, a separate group of specimens were processed for the purpose of microscopy.
As for the organic acid fluxes, their solubility in water determined the following cleaning scenario:

1. Rinse ultrasonically 4 min in hot tap water, and repeat with a fresh volume of water.
2. Immerse 3 min in agitated deionized water.
3. Rinse 75 sec in acetone.
4. Dry with $N_2$ gas.

A final note on flux cleaning. The above procedures were ineffective not only on samples allowed to remain uncleaned for times in excess of 1 day, but also (to a limited extent) on coupons tested at high temperatures, particularly above 260°C. Char residues from both the organic fluxes (black-brown-colored) and the rosin-based flux (the usual white and tan-colored deposits)[8–10] were unaffected by the solvents and rinses unless removed immediately after testing.

## 2.5 Testing Procedures

It is important to point out that the testing conditions between the meniscometer and the wetting balance were kept exactly the same in order to correlate the data from the two separate tests and calculate the contact angle. Therefore, parameters such as solder temperature and dwell time had to be consistent for the two procedures. The meniscometer and wetting balance solder baths were maintained to within $\pm 1$°C of each other.

***2.5.1 Meniscometer Tests***—The objective of the meniscometer was to determine the distance risen by the solder up the coupon surface. A schematic of the meniscometer is shown in Figure 10a. The absolute error on the measurements was $\pm 0.002$ cm, which arose mainly from the initial zeroing of the microscope to the solder surface. A brief description of the testing process follows. First, the traveling microscope was zeroed to the surface of the solder and then focused and aligned to the vertical plane of the coupon. Next, the coupon to be tested was placed into the sample holder that had been previously adjusted to allow for the same immersion depth as used in the wetting balance. The coupon was allowed to sit $\sim 1$ cm above the solder bath for 30 sec. Then the coupon was lowered into the solder where it remained for 20 sec. The meniscus height was recorded at that time, after which the sample was removed. This procedure was repeated for the other three coupons of the set. The meniscus height was determined by the average of those four values; the error was taken as one standard deviation ($1\sigma$) of the data.

***2.5.2 Wetting Balance Tests***—The purpose of the wetting balance was to obtain the weight of the solder in the risen meniscus. A schematic of this apparatus is shown in Figure 10b. The signal derived from the microbalance was transmitted to the computer, where it was stored and analyzed to give the meniscus weight values necessary for the calculation of the contact angle. An example of the generic wetting balance curve is shown in Figure 11. Schematics of the physical interpretation of those features of the wetting curve designated by points A, B, and C appear in the insert. In addition to the maximum meniscus weight, W, necessary to calculate the contact angle, the wetting rate, $\dot{W}$, and the time to reach the maximum meniscus weight, $t_W$, are also determined from the plot. Both parameters find their importance tied to the production of the joint in terms of how quickly the assembly can be joined and still establish a fully wetted substrate. The value of $t_W$ is calculated as the time at which the wetting curve reaches the value of the meniscus weight, W. The wetting rate is determined from the slope of the optimally visualized straight-line fit to the curve from the point at which

the coupon experiences only the buoyancy force,(ID) (point B in the figure), to the point where the plot begins to deviate from a linear trend. Recording the wetting rate directly from the initial data output implies that the effects of the time-dependent part of the buoyancy force resulting from the rising meniscus were not included. It was confirmed that the time-dependent buoyancy force contribution had a negligible effect on the wetting rate calculations.

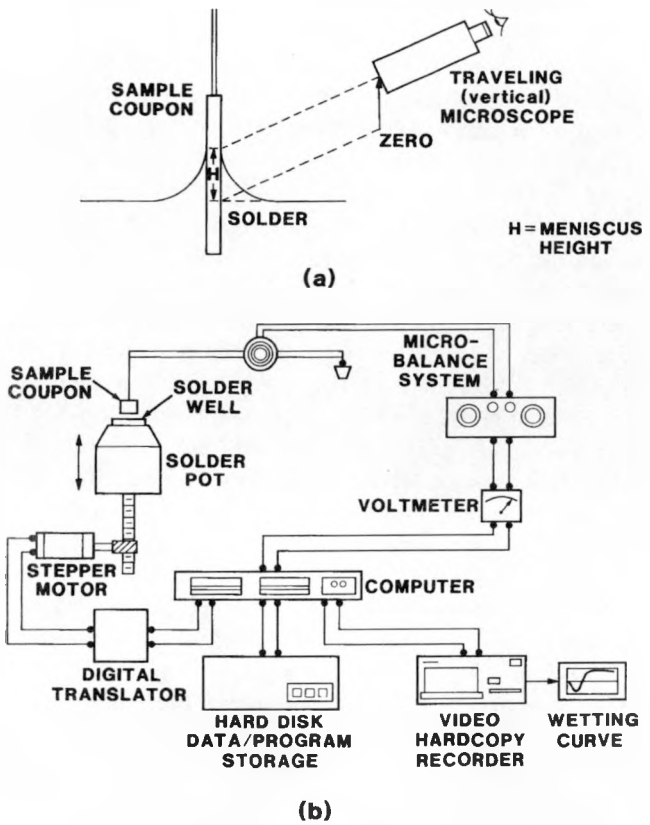


**Figure 10.** Solderability Testing System (a) Meniscometer schematic (b) Wetting balance system schematic.

Finally, we emphasize that the wetting rate is the rate of increase in the meniscus weight. This calculation can also be used to obtain the rate change in the contact angle as wetting proceeds. Although the kinetics of wetting have been analyzed by the change in the meniscus weight (more precisely, the wetting force as defined by the meniscus weight divided by the coupon perimeter),[11–13] it is not yet clear which parameter more accurately describes the physical process of wetting.

Movement of the heater pot that determined the rate and depth of immersion of the coupon into or out of the solder was controlled by a programmable indexer that directed a stepper motor attached to the pot (Figure 10b).

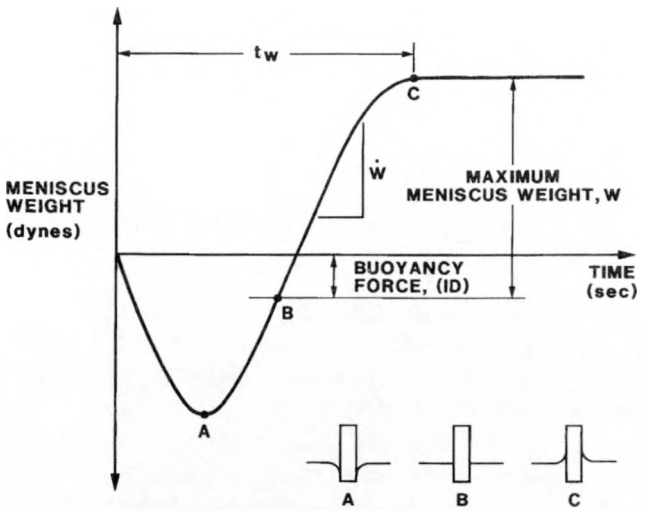


**Figure 11.** The typical wetting curve of meniscus weight as a function of time. The insert describes the meniscus behavior responsible for particular artifacts of the plot.

Calibration of the microbalance voltage output was performed with a set of tare weights ranging from 20 to 1000 g. This calibration determined the scale factor for converting the voltage signal to the measurement of force. A second calibration was performed to verify that the hardcopy output of weight equaled the weight of the calibration masses.

For all wetting balance tests, the coupon was immersed at a rate of 1.3 cm/sec. The nominal immersion depth was $0.38° \pm 0.02$ cm. As with the meniscometer data, the immersion time for each coupon was 20 sec. The error in measuring the meniscus weight arose from the signal noise generated in the electronics of the microbalance and computer, resulting in an absolute error of $\pm 30$ dyn.

A brief description of the testing procedure follows. The fluxed coupons were suspended from the balance above the solder bath for ~30 sec. As with the meniscometer measurements, the dross was cleaned from the solder surface before immersion. The solder surface was brought up to within 0.025 cm of the sample, at which point the stepper motor was engaged to move the pot upwards another 0.40 cm to immerse the specimen, giving rise to the nominal immersion depth of 0.38 cm. At the moment the solder contacted the coupon, an electrical signal was sent to the computer to commence data acquisition. After a 20-sec dwell period, the solder pot was lowered and the test completed. The maximum value of W was measured as the average value between 10 and 20

sec of testing. The meniscus weight was taken as the average of the six tests; the indicated absolute error was 1 $\sigma$ of those results.

Together, the average meniscus height and the average meniscus weight are introduced into Eq (7) to calculate the value of $\gamma_{LF}$; it was also substituted into Eq (8) to determine the contact angle. The indicated absolute error on $\gamma_{LF}$ and $\theta_c$ was the maximum and minimum values based on the range of numbers of the meniscus height and weight established by $\pm 1\sigma$ about each parameter mean.

***2.5.3 T-Peel Sample Assembly and Pull Tests—*** The T-peel pull samples were assembled on a copper platen placed on a hot plate. A thermocouple probe was inserted into a hole in the copper platen to accurately determine its temperature. The platen temperature was allowed to reach 268°C ± 2°C before sample assembly. In the assembly procedure, a 60Sn40Pb solder preform measuring 1.58 × 2.54 cm was placed onto the flat copper sheet where it had been fluxed. Then the cleaned and fluxed Kovar piece was placed atop the solder so as to precisely cover the preform. With a preload of 20 g placed on the Kovar, the entire assembly was transferred to the copper platen surface atop the hot plate. For nearly every sample, reflow of the solder was completed in 20 to 25 sec as determined by the formation of the solder fillet around the entire perimeter of the Kovar leg. Nevertheless, the sample was maintained on the hot plate for 45 sec to allow for adequate heating of the Kovar (as a heat sink was formed by the 20-g mass) and for the removal of gaseous flux and air.

Prior to pull testing, the excess copper sheet was trimmed away from the Kovar. Then, the T-peel sample was cut in half so that the dimension, L, became 1.27 cm, thereby allowing for 10 test samples. Finally, the copper was bent so that, with the Kovar, the final T-peel-shaped sample was fabricated.

Pull tests on the T-peel specimens were conducted on an Instron tensile tester. The rate of displacement was 5.08 cm/min. Test curves similar to those in Figure 5b were obtained in these tests and analyzed as described earlier. In most cases, 4 of the 10 pull samples were tested.

# 3. Results

## 3.1 The Effect of Cleaning Procedures on Solderability

As alluded to in Chapter 2, the cleaning-fluxing-testing sequence inherently led to slightly different conditions for each of the five samples making up a batch. Because of the extreme sensitivity of wetting phenomena to surface conditions and impurities, observations were made to determine whether a particular coupon's place in the cleaning sequence affected its wettability for the given flux and solder.

First, the meniscometer data were examined. For these samples, the time period between fluxing and testing showed the greatest difference (13 min) between the first and fifth samples. The interval between cleaning and fluxing was negligibly different for the coupons. From the data for each flux, no trend beyond the experimental error could be detected that indicated a dependence of the meniscus height on the difference of time periods between fluxing and testing.

As for the wetting balance data, differences in the fluxing-to-testing period ranged from ~6 to 22 min. Except for the Alpha™611 flux, Diversey etch, and plain Kovar case, no trend distinguishable from the experimental error was observed between the meniscus weight and the difference of time periods. As for the Alpha™611 study, the weight increased only slightly with time. However, the use of A611 on both electropolished, plain Kovar and the gold-nickel-plated Kovar showed no such trend. This analysis indicates that the cleaning, fluxing, and testing logistics had a generally negligible influence on the solderability results.

Finally, we noticed in the experimental details that one of the wetting balance coupons was cleaned with the meniscometer samples and not with the other five wetting balance specimens. From the analysis described in the previous paragraph, no differences in the meniscus weight were noted between the coupons cleaned in different batches. We conclude that the use of two different cleaning baths did not affect the requirement of identical testing conditions for all samples of the particular run.

## 3.2 Solderability As a Function of Flux

***3.2.1 Diversey Surface Etch—Plain Kovar—*** Table 2 shows the solderability data obtained for plain Kovar coupons cleaned by the Diversey surface etch, coated with one of the five fluxes, and dipped into the solder held at 260°C. Also included are the results of the nickel-plated and gold-nickel-plated Kovar. The error terms associated with the data in this table provided important information of the solderability behavior of each flux. As the contact angle increased, so did the uncertainty of the data. Referring to the

plain Kovar results in Table 2, we see that the wetting rate, $\dot{W}$, and the time to maximum meniscus weight, $t_W$, did not exhibit a behavior similar to that of the contact angles. The gold-nickel- and nickel-plated coupons showed values of $\theta_c$ well below those of the plain Kovar specimens, regardless of the flux. Moreover, a very fast $\dot{W}$ and shorter $t_W$ were recorded on the gold-nickel-plated samples when compared to the plain Kovar data for similar fluxes. A comparison of the nickel-plated and plain Kovar data shows that use of B1452 caused higher values of $\dot{W}$ and $t_W$ for the plated samples. The use of A611 caused an increase in $\dot{W}$ and a decrease of $t_W$ when the nickel plating was added to the coupons.

Figure 12 shows representative curves from (1) the wetting balance tests for each flux used on the plain Kovar coupons and (2) the two sets of plated samples. The use of A250HF and A611 on plain Kovar resulted in an initial negative meniscus weight similar to that in Figure 11. Although B1452 showed no negative weight for plain Kovar, a small degree was recorded on the nickel-plated Kovar. The application of A611 to the gold-nickel-plated samples resulted in immediate wetting; no negative meniscus weight was detected.

Several of the wetting curves in Figure 12 show that the meniscus weight reaches a maximum value and then diminishes somewhat. This may have been caused by a change to the solder-substrate interface metallurgy as it affects $\gamma_{SL}$. It is not likely that this phenomenon was caused by temperature-related changes to the flux[8] or by solder-flux interface (which would influence $\gamma_{LF}$),[9-10] or even by volatilization of flux components since the meniscus weight drop was not observed with the plain Kovar coupons under the same testing conditions. The largest magnitude of this effect was recorded for the gold-nickel-plated samples and probably indicates changes in the solder-substrate interfacial tension as the plating dissolves into the solder[14].

**Table 2. Solderability data of the 2-min Diversey-etched, plain Kovar and plated Kovar samples**

| FLUX[1] | $\theta_c$ deg | $\gamma_{LF}$ dyne/cm | $\gamma_{SF}-\gamma_{SL}$ dyne/cm | $\dot{W}$ dyne/sec | $t_w$ sec |
|---|---|---|---|---|---|
| | | | PLAIN KOVAR | | |
| B1452 | 29±5 | 430±30 | 380±10 | 1290±50 | 3.2±0.2 |
| A260HF | 45±6 | 510±90 | 360±20 | 1400±100 | 2.5±0.2 |
| B2508 | 53±5 | 540±80 | 325±15 | 1390±150 | 2.8±0.2 |
| A250HF | 53±11 | 290±100 | $175^{+0}_{-30}$ | 600±100 | 3.8±0.5 |
| A611 | 61±11 | 650±200 | $315^{+0}_{-40}$ | 1230±50 | 4.7±0.3 |
| | | | NICKEL-PLATED KOVAR | | |
| A611 | 24±2 | 380±20 | 350±15 | 1300±150 | 3.97±0.06 |
| B1452 | 24±3 | 480±30 | 440±15 | 1330±20 | 4.4±0.9 |
| | | | GOLD-NICKEL PLATED KOVAR | | |
| A611 | 11±5 | 360±30 | 350±20 | 1490±50 | 2.0±0.2 |
| B1452 | 15±3 | 460±20 | 440±10 | 1670±200 | 2.3±0.2 |

[1]FLUX DILUTED 1:1 BY VOLUME WITH ISOPROPYL ALCOHOL

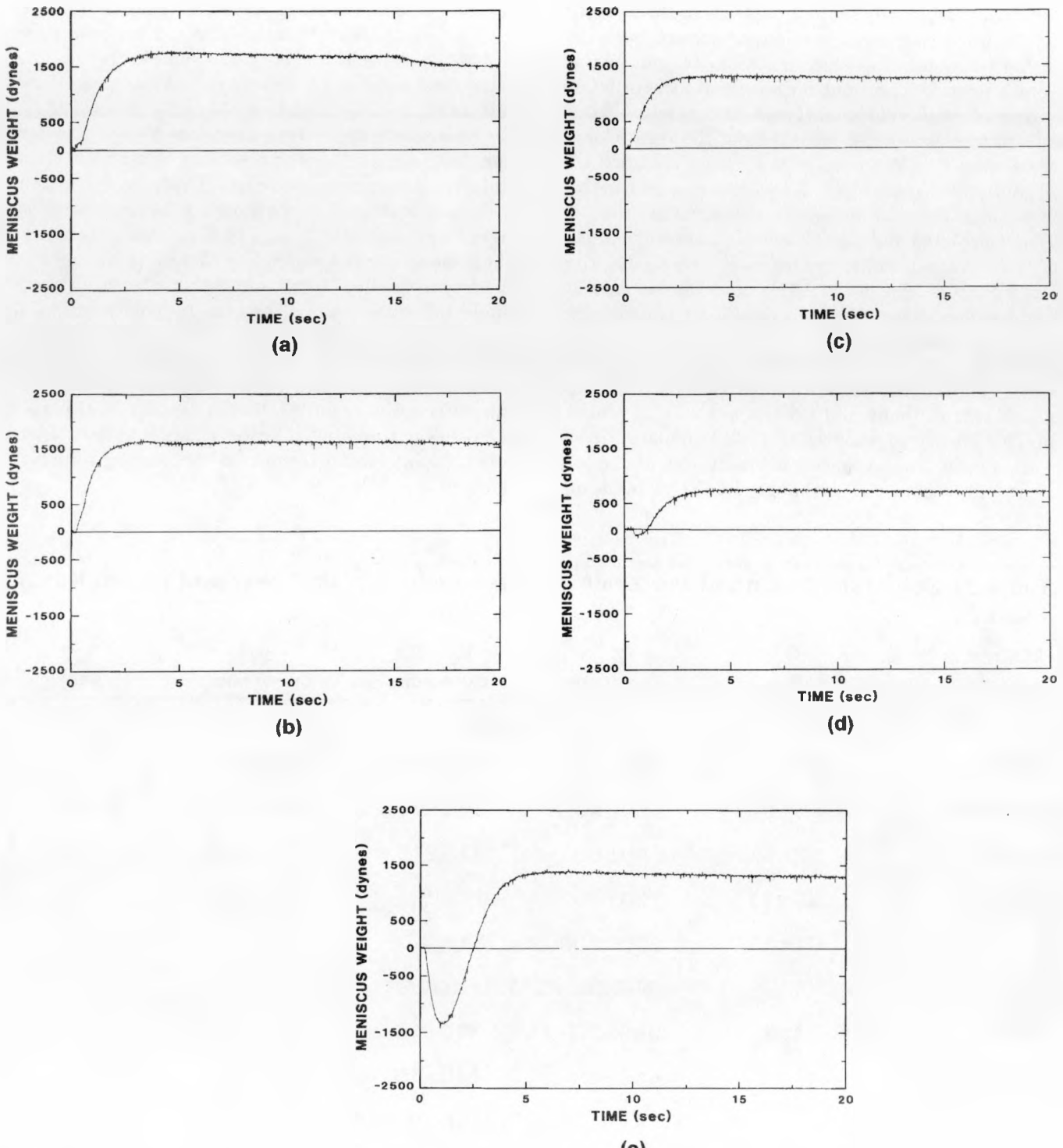


**Figure 12.** Representative wetting curves of the 2-min Diversey-etched, plain Kovar samples and plated coupons as a function of the different fluxes. The solder temperature was 260°C and all fluxes were diluted 1:1 by volume with isopropyl alcohol. Plain Kovar data: (a) B1452, (b) A260HF, (c) B2508, (d) A250HF, and (e) A611. Nickel-plated Kovar: (f) A611, and (g) B1452. Gold-nickel-plated Kovar: (h) A611 and (j) B1452.

(continued)

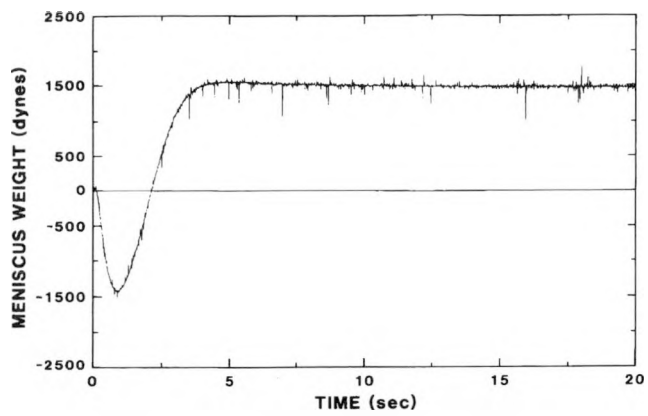


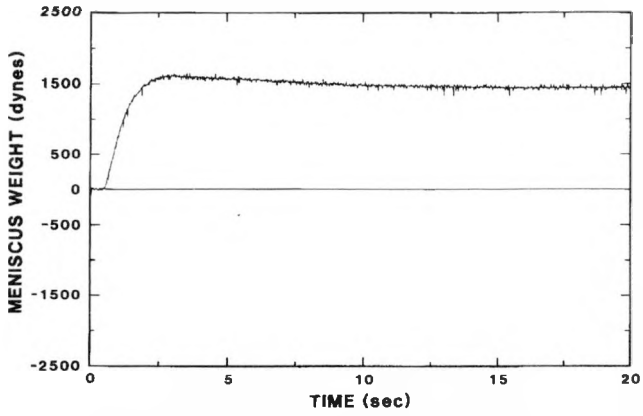


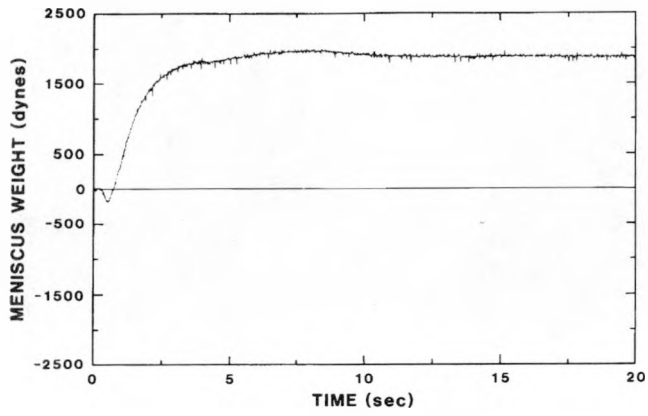


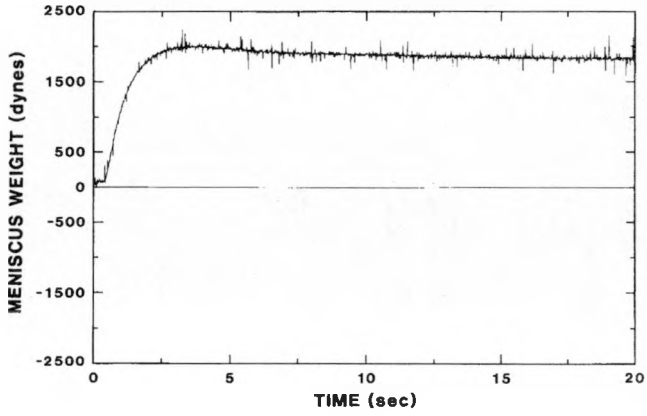


**Figure 12.** (concluded)

For some of the plain Kovar coupons fluxed with A611, the solder did not wet some parts of the surface at all. The wetting balance curve and a photograph of the specimen surface of one such instance are shown in Figure 13. This phenomenon was also recorded with the B2508 and A250HF fluxes but was never observed with the B1452 nor with the A260HF fluxes.

Also shown in Table 2 are the solder-flux interfacial tensions, $\gamma_{LF}$, and the interfacial tension differences, $(\gamma_{SF}-\gamma_{SL})$ as described by Young's equation. Note that $\gamma_{LF}$ depends strongly on the type of flux. Moreover, the contact angle was dramatically affected by $\gamma_{LF}$ and not just by the Kovar surface conditions described by $(\gamma_{SF} - \gamma_{SL})$.

Outlined in Table 3 is an evaluation of the flux residues noted on the samples as a function of the flux.

Qualitative observations of the solder front—that is, the top of the risen meniscus—were made using optical microscopy and scanning electron microscopy (SEM). Shown in Figure 14 is an SEM micrograph (secondary electron emission) of the solder front on plain Kovar that had been cleaned by means of the Diversey treatment and fluxed with A611. Optical micrographs of the cross section of the solder film showed a gradual diminishing of the film thickness as the solder front was approached (Figure 14). The "butterfly" pattern of the lead-rich phase was observed for each flux. Although severe grain boundary attack resulted from the Diversey treatment, preferred wetting of the grain boundaries was not observed with the use of A611. Such preferred wetting of the grain boundaries *was* observed on plain Kovar with the use of the flux B1452 (Figure 15a). The backscattered electron image (not shown), which more clearly delineates different elements through contrast differences based on atomic number (light areas are lead-rich; dark areas are tin-rich), indicated that the tin-rich phase preferentially wetted the grain boundaries. The blackened spots on the solder film were a result of flux residue. Porosity caused by the volatility of the flux on heating is visible in the optical micrograph of Figure 15b. Like the A611 results, the

solder film gradually thins as the top of the meniscus is reached.

Grain boundary wetting was also observed for plain Kovar fluxed with A260HF. Small pores and burnt flux residue were also noted. In addition, the actual solder film edge had a very steep profile for a distance of ~15 μm from the tip of the meniscus (Figure 16a). A schematic of the profile in Figure 16b demonstrates the variations in film thickness. A similar solder film profile was recorded for A250HF. But for both the A250HF and A260HF fluxes, the steep solder film profile *disappeared* when the Kovar was cleaned by means of the electropolishing procedure; the meniscus film appeared to be very similar to the A611 flux in Figure 14. No unusual features were observed in the solder film phase distribution morphology in the case of each flux.

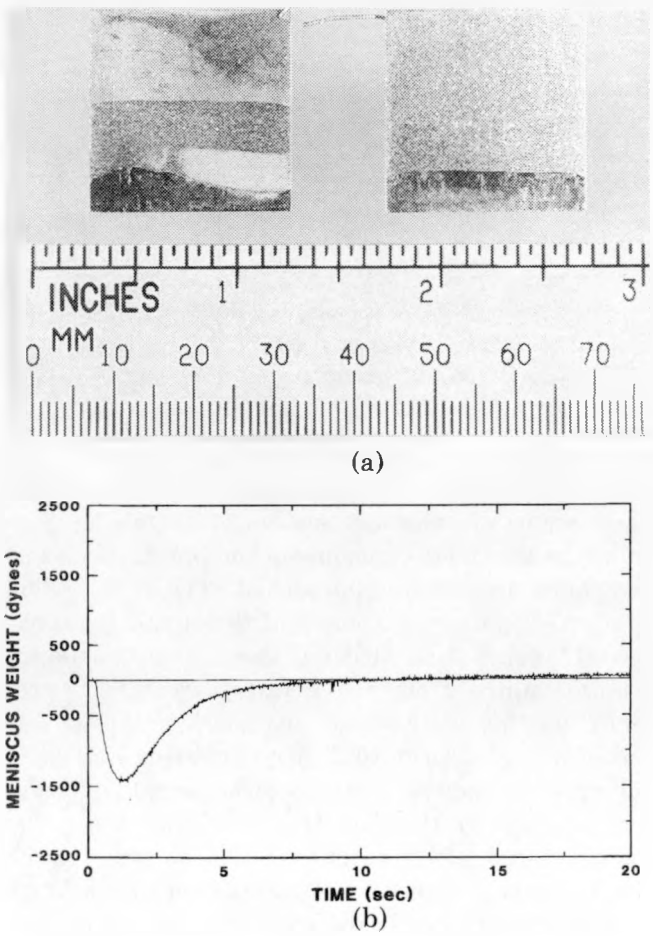


**Figure 13.** Solder film on a nonwetting sample; so designated by the refusal of the solder to completely rise up the coupon (2-min Diversey etch, 260°C, A611). (a) On the left is the coupon, and on the right a normally behaving sample. (b) The wetting curve of the nonwetting sample.

**Table 3. Qualitative evaluation of the flux residues on Diversey-etched, plain Kovar coupons**

| FLUX | RESIDUE PARAMETER |
|---|---|
| A611 | 0 |
| A250HF | 2 |
| B2508 | 5 |
| A260HF | 6 |
| B1452 | 10 |

SCALE: 0, 1, . . . 10
BEST WORST

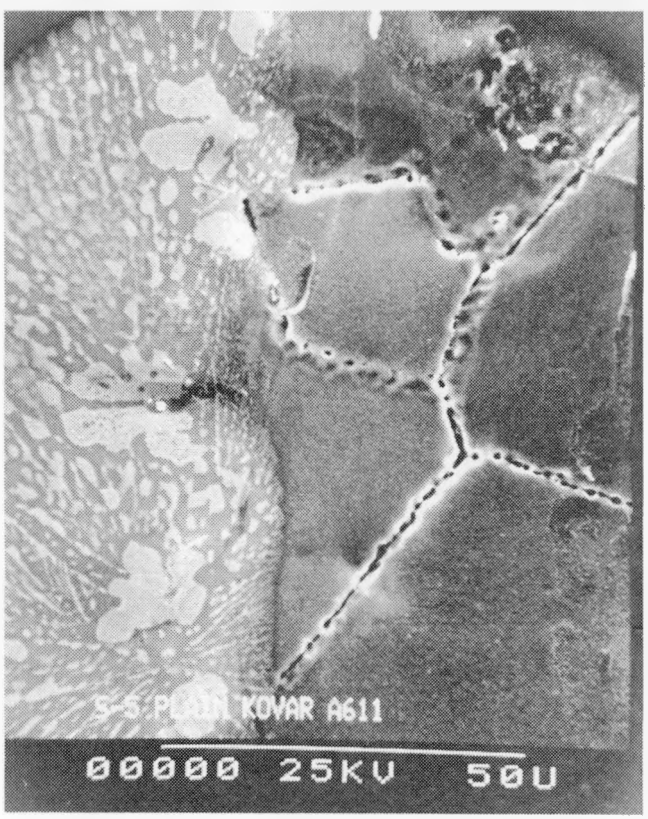


**Figure 14.** SEM micrograph (secondary electron) of the meniscus front on a 2-min Diversey-etched, plain Kovar coupon fluxed with A611. The solder layer is to the left and the Kovar surface to the right. The magnification and accelerating voltage appear at the bottom.

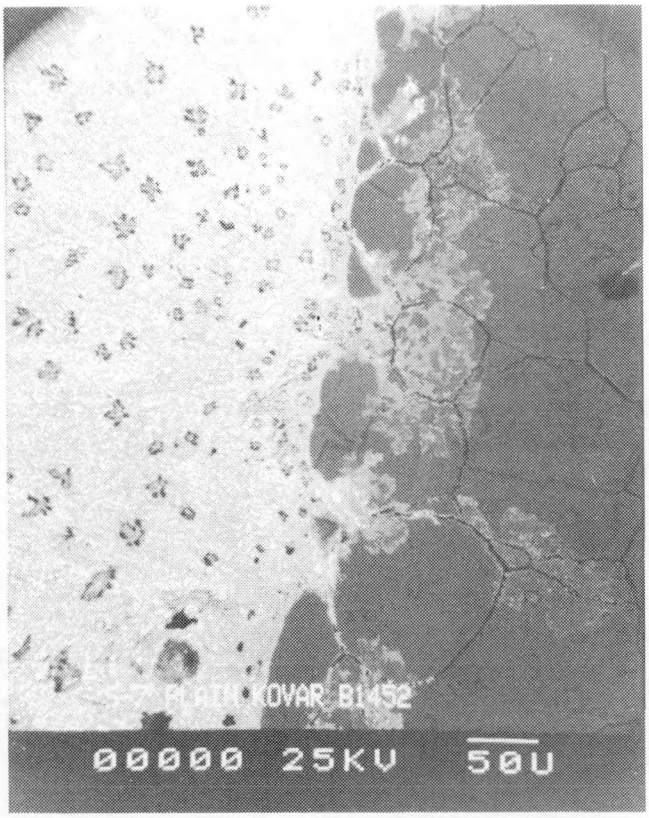


(a)

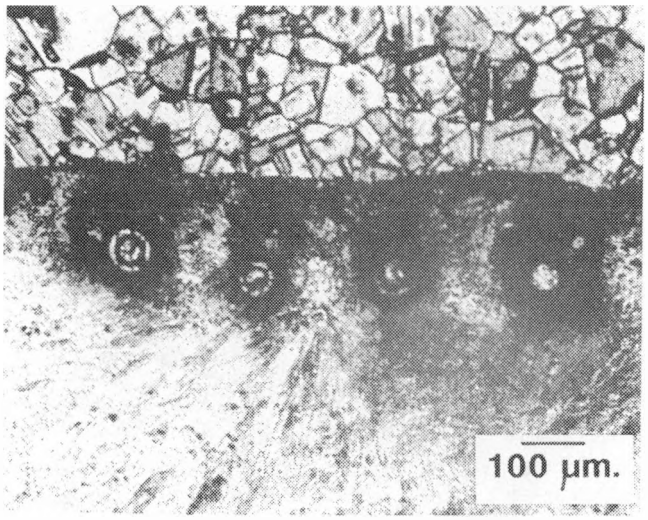


(b)

**Figure 15.** SEM micrograph (secondary electron) of the meniscus front on a 2-min Diversey-etched, plain Kovar sample fluxed with B1452. (a) The solder film is to the left, the Kovar surface to the right. (b) Optical micrograph (differential interference contrast) of the porosity generated on a similarly tested coupon.

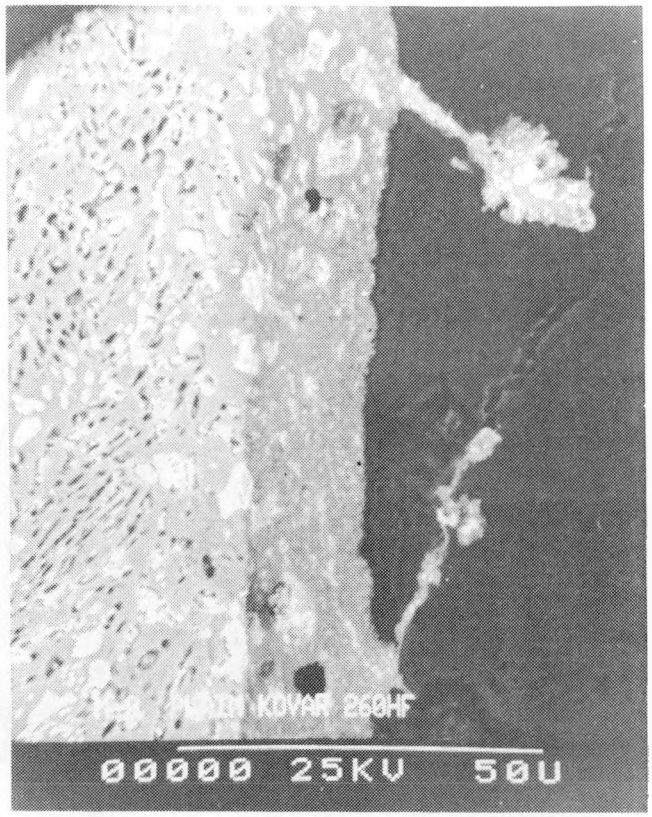


(a)

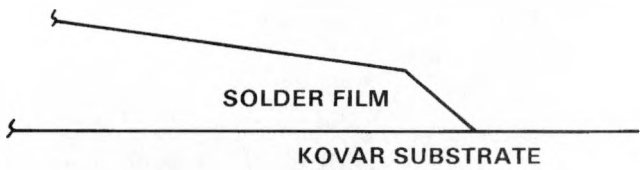


(b)

**Figure 16.** SEM micrograph (backscattered electron) of the solder front on a 2-min Diversey-etched, plain Kovar sample fluxed with A260HF. (a) The solder film is to the left, the Kovar surface to the right. (b) Schematic of the solder film in profile showing the change of slope.

For the flux B2508, extensive grain boundary wetting was noted as shown in the SEM (secondary electron image) (Figure 17). Porosity and flux residues appear in this image as diffuse, gray regions on the solder film. Also, the grain boundary wetting by the solder appeared to have been the most extensive for this flux as compared to A260HF and B1452.

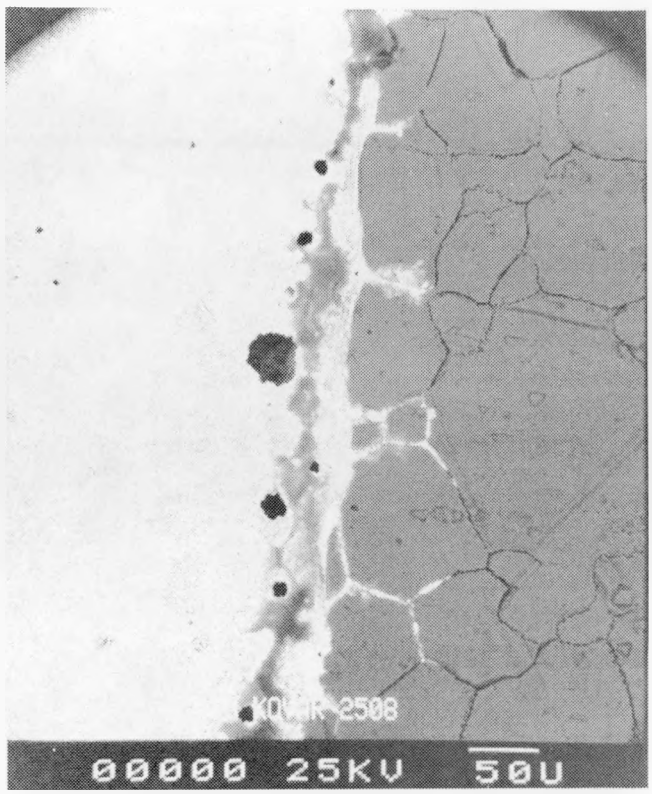


**Figure 17.** SEM micrograph (secondary electron) of the meniscus front on a 2-min Diversey-etched, plain Kovar sample fluxed with B2508. The solder film is to the left; Kovar surface to the right. Note the grain boundary penetration by the solder.

Observations of the solder film produced by the wetting of plain Kovar with A611 showed extensive dewetting; see the optical micrograph in Figure 18. Unlike the case of incomplete wetting in Figure 19, dewetting takes place after the solder has initially wet the surface. When the coupon is withdrawn from the solder pot, the solder layer collects into mounds of material (Figure 18a) leaving a very thin layer of solder on the remaining surface (Figure 18b). Localized regions around some small particles were free of a solder film.

Electron microprobe analysis was performed on cross sections of the solder films to detect dissolution of the elemental components of Kovar (namely, iron, nickel, or cobalt) by reaction with the tin component of the solder.[15] Concurrent SEM analysis was used to investigate the presence of interfacial cracking between the solder film and the substrate. Shown in Figure 20 is an SEM (backscattered electron) image of the solder film cross section of a plain Kovar sample, Diversey-cleaned and fluxed with B1452. The light areas are lead-rich; the dark regions, tin-rich; and the intermittent black particles are either organic residues from the flux or small voids. No interfacial cracks nor unusual distribution of the solder phases were observed. In addition, the grain boundary penetration (wetting) by the solder observed in Figure 15a was relatively shallow since it was not observed in any of the cross-sectional views in the microprobe analysis. X-ray maps of iron, nickel, and cobalt from the exact same location as that shown in Figure 20 showed no significant traces of the three elements in the solder film. A similar analysis was also performed on a Kovar coupon fluxed with A611, with the same results.

By using the B1452 flux, we varied the time period during which the plain Kovar coupons were exposed to the chemical etchant to between 0 and 4 min. The results are outlined in Table 4. A new batch of test samples was used for the 2-min etch; hence the slight variation from the B1452 data in Table 2. The minimum value of $\theta_c$ was achieved with the 2-min etching time. The behavior of $\theta_c$ was more sensitive to the interfacial tension, $\gamma_{LF}$, than to $(\gamma_{SF} - \gamma_{SL})$. As expected, no wetting took place on samples that received no surface treatment. The value of $\dot{W}$ was a maximum and that of $t_W$, a minimum, for the 2-min. etch. Otherwise, the parameters $\dot{W}$ and $t_W$ demonstrated no apparent trend with etching time nor with the other solderability parameters.

***3.2.2 Gold-Nickel-Plated and Nickel-Plated Kovar***—The solder film on a nickel-plated coupon was examined by the SEM; a micrograph (backscattered electron image) is shown in Figure 21. Ahead of the main body of the solder film, a thinner region of solder is located; it comprises both lead- and tin-rich phases. This "prefilm" of solder was shown in optical micrographs to exist along most of the solder front length. It appeared to be much more extensive with the use of B1452 than was observed when the sample was fluxed with A611. Also, the nickel plating was incomplete in some regions of the coupons. This had a direct effect on the wettability of the solder (Figure 22) because the solder would not wet those regions without the nickel film, as indicated by the large "hill" of solder caused by a larger contact angle. Recall that these samples were simply degreased, an ineffective procedure for sufficiently cleaning the plain Kovar surface (i.e., where the plating was absent) and allowing wetting by the solder.

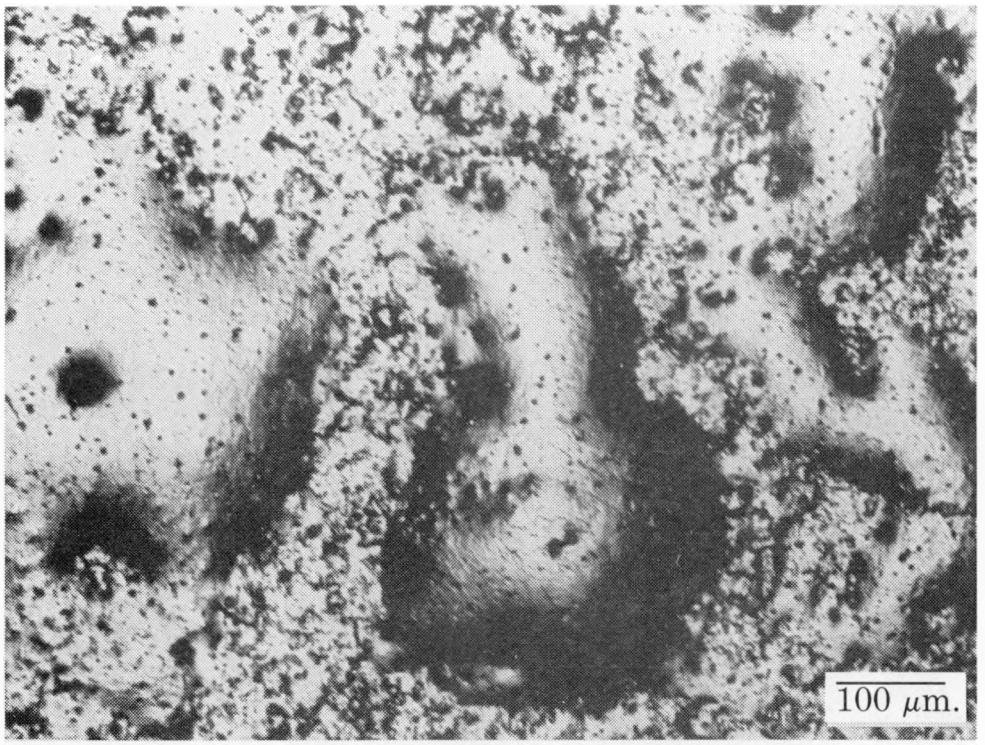


(a)

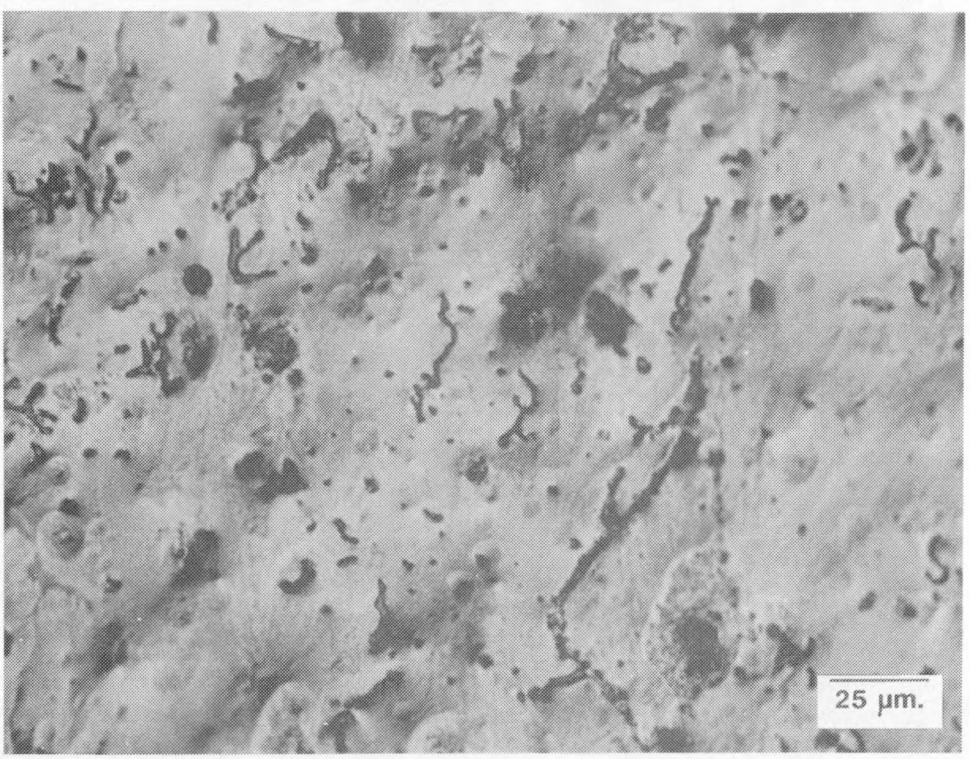


(b)

**Figure 18.** Optical micrograph (differential interference contrast) of a 2-min Diversey-etched, plain Kovar sample fluxed with A611. (a) Dewetted sample (b) High magnification of the dewetted region between solder mounds.

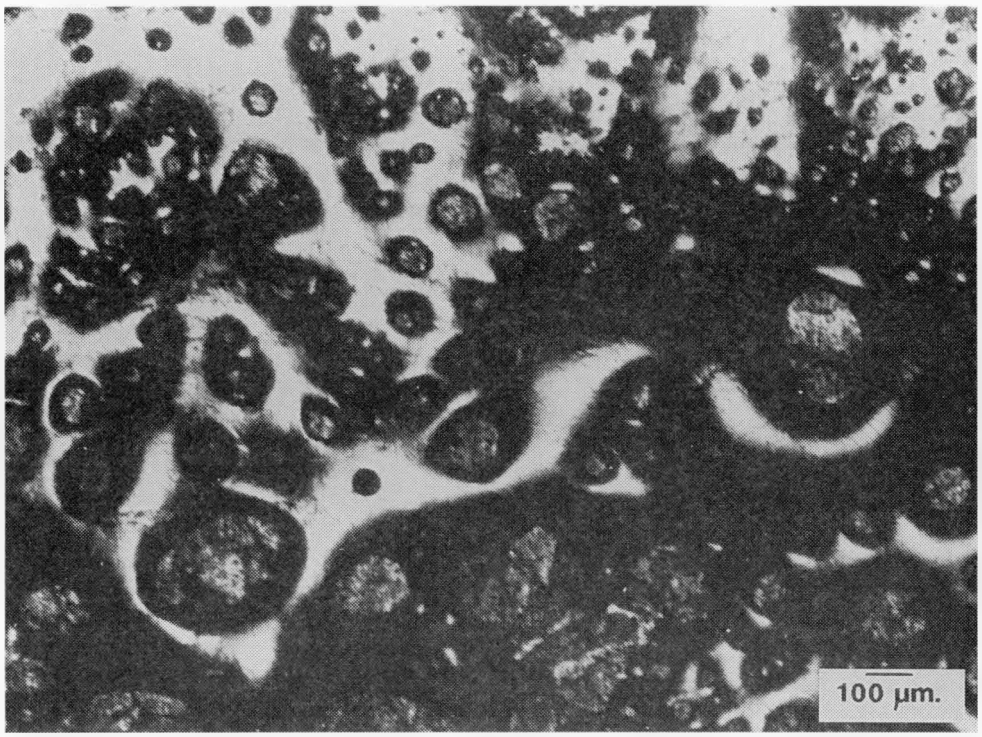


**Figure 19.** Optical micrograph (differential interference contrast) of incomplete wetting on a plain Kovar sample that was only *degreased* before fluxing with B1452.

Figure 23 shows an optical micrograph of the solder film on a sample of gold-nickel-plated Kovar fluxed with A611. Three distinct zones of morphology are found on the solder film. The first zone at the very edge of the film is seen in Figure 24a. The second zone shows a smooth topography, while the third zone exhibits a series of striations caused by the growth of gold-tin intermetallic crystals. A higher-magnification photograph of those intermetallic crystals is shown in Figure 24b. Beyond the third zone and towards the bottom of the coupon, the intermetallic crystal morphology disappears and a uniform solder film is observed as seen on the plain Kovar samples. Note that the morphology depends on the type of flux used during the tinning process. For example, Figure 25 shows the solder film of a gold-nickel-plated specimen on which no flux was applied, while Figure 26 shows the same type of coupon fluxed with B1452. As with the use of A611, the latter two cases exhibit extensive arrays of gold-tin intermetallic growth. With the absence of any flux (Figure 25), a large number of gold particles were visible on the solder surface, thereby making the morphology difficult to observe. For the case in which the B1452 was applied (Figure 26), two regions were noted: The first was a "rough" morphology located at the film edge and extending back to the second region of intermetallic crystal formation. Some slight variations to the first zone were noted at several locations on the solder film front.

Cross sections of the gold-nickel- and nickel-plated coupons were investigated by election microprobe. Shown in Figure 27 is the SEM image of the solder film on a nickel-plated coupon. Several large, black regions ($\sim$10 $\mu$m) were observed; they were the result of chemical compositions other than the expected lead- and tin-rich phases. The small, black areas ($<$1 $\mu$m in diameter) were predominantly the result of organic residues or voids (as assessed by comparison with the corresponding secondary electron image). Figure 28a shows the nickel x-ray map of the same location. The nickel layer on the exposed solder film surface was applied as part of the metallurgical preparation of the sample. Clearly, nickel was present in those large, dark regions of Figure 27. When we compare the x-ray map of tin, Figure 28b, with Figure 28a, we note that tin was also found in the regions occupied by the nickel. Lead was absent in these locations. Quantitative analysis of the nickel-tin regions showed them to be 42.3° $\pm$ 0.5 a/o nickel and 57.7° $\pm$ 0.5 a/o tin (the error is 1$\sigma$). These amounts correspond to the formation of $Ni_3Sn_4$ intermetallic.

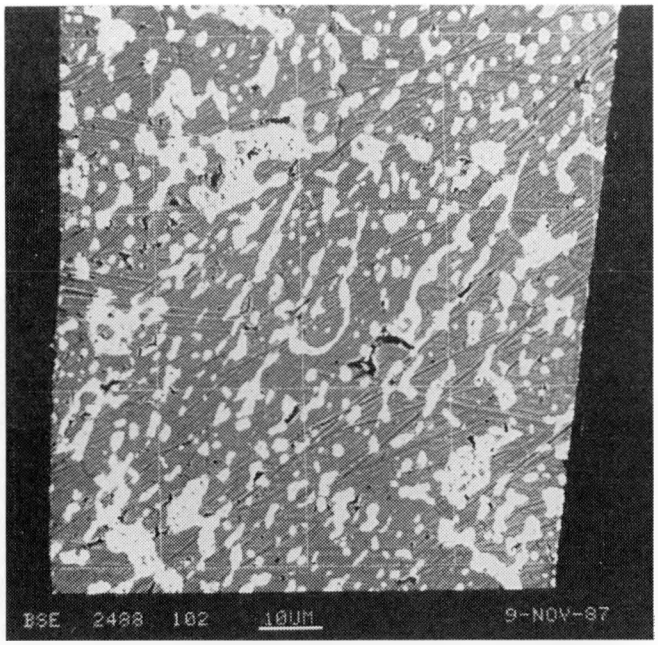


**Figure 20.** SEM micrograph (backscattered electron) of the solder-film cross section of 2-min Diversey-etched, plain Kovar sample fluxed with B1452. The Kovar coupon is to the left and the solder-film-free surface (which has been nickel-plated) is to the right. The lighter regions are the lead-rich phase; the darker regions, tin-rich. The magnification appears at the picture bottom.

**Table 4. Solderability data on plain Kovar for different Diversey-etching periods**

| CHEMICAL ETCHING TIME min | $\theta_c$ deg | $\gamma_{LF}$ dyne/cm | $\gamma_{SF} - \gamma_{SL}$ dyne/cm | $\dot{W}$ dyne/sec | $t_w$ sec |
|---|---|---|---|---|---|
| 0 | ~180 | — | — | — | — |
| 0.5 | 48±10 | 530±150 | $355^{+5}_{-55}$ | 1050±50 | 3.9±0.7 |
| 1.0 | 39±10 | 450±100 | $350^{+10}_{-50}$ | 980±150 | 4±1 |
| 2.0 | 32±5 | 420±40 | 360±15 | 1260±150 | 3.0±0.6 |
| 4.0 | 34±3 | 460±30 | 380±10 | 1250±20 | 4.3±0.3 |

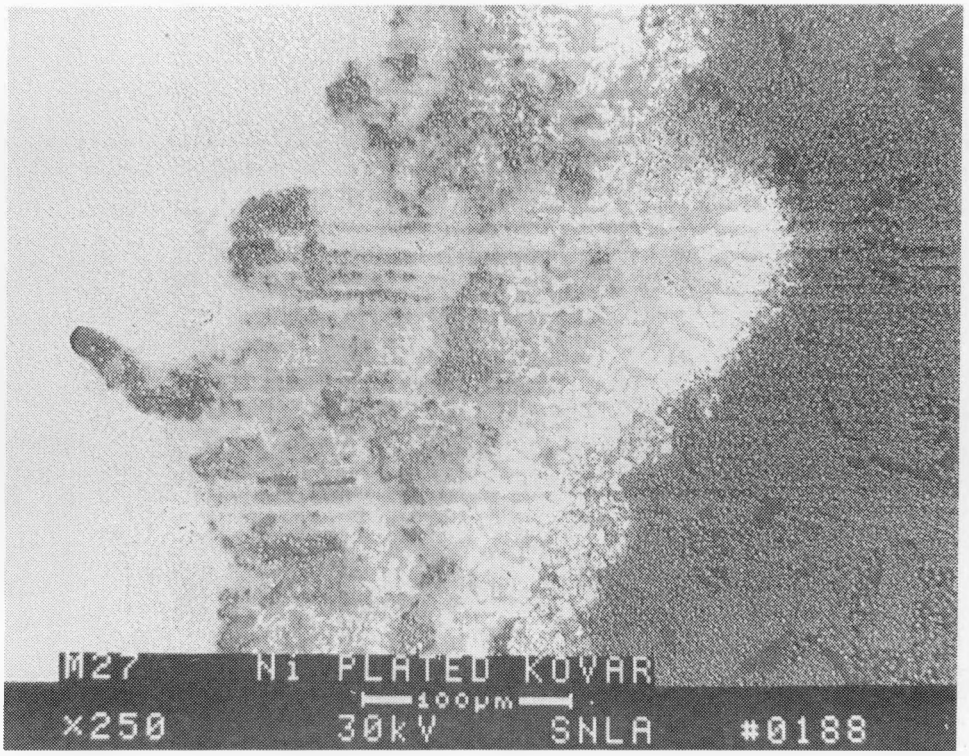


**Figure 21.** SEM micrograph (backscattered electron) of the solder-film edge on a nickel-plated Kovar sample fluxed with B1452. The solder-film is to the left; the plated surface to the right.

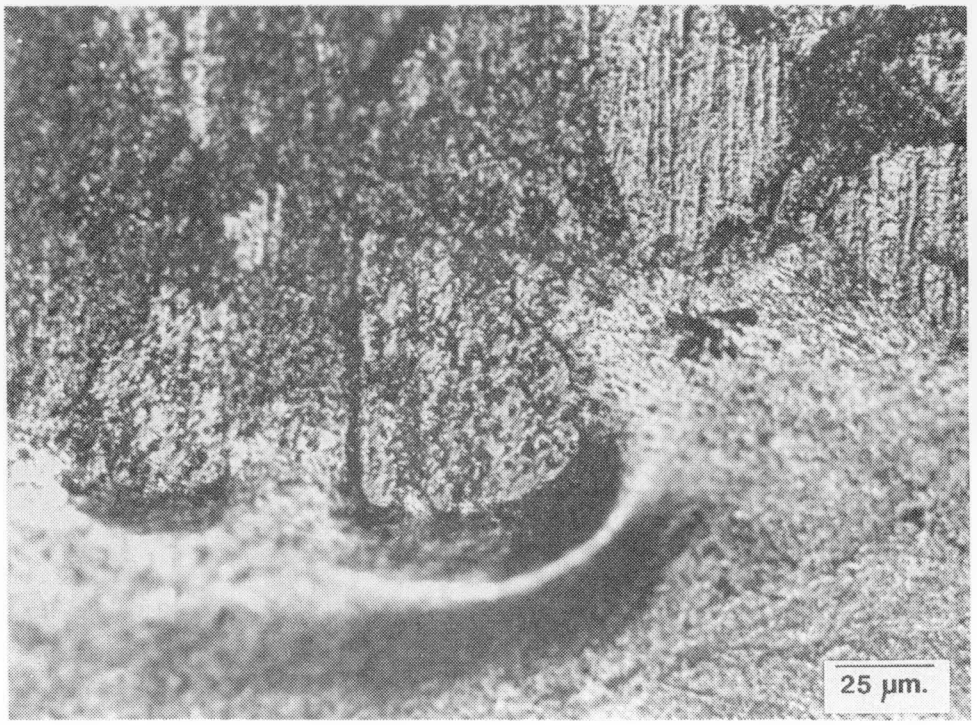


**Figure 22.** Optical micrograph (differential interference contrast) of the solder front on a nickel-plated Kovar coupon fluxed with B1452. The solder film is on the bottom; the plated surface, on top where the lighter regions are the unplated bare Kovar.

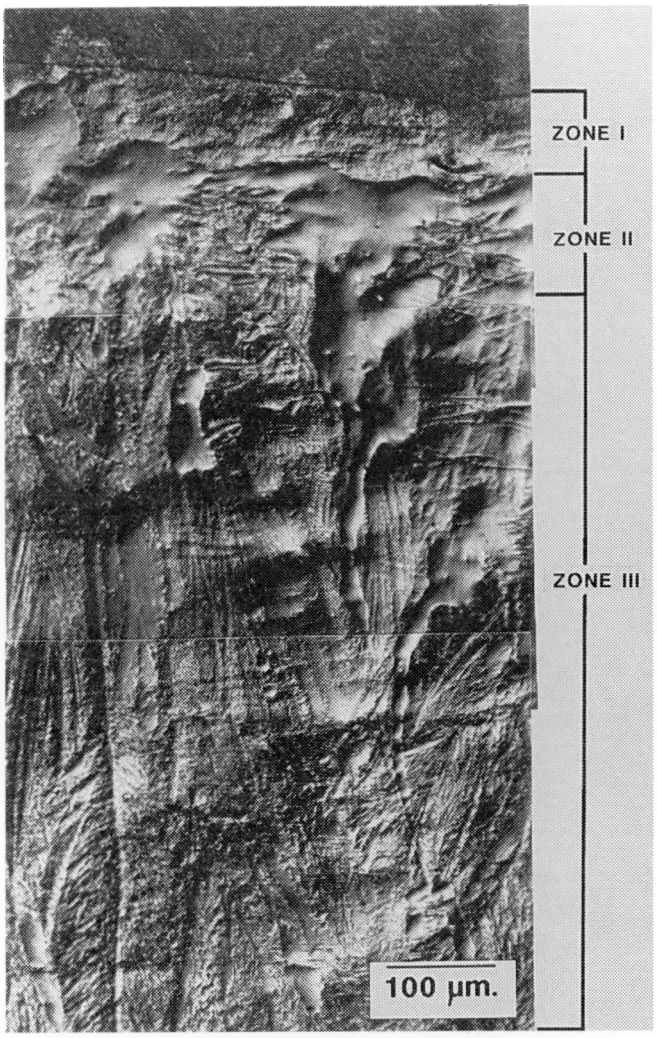


**Figure 23.** Optical micrograph (differential interference contrast) of the solder film on the gold-nickel-plated coupon fluxed with A611. The three zones of distinct morphologies have been marked.

Electron microprobe analysis was performed on the gold-nickel-plated Kovar samples fluxed with A611. A solder film layer ~22 μm wide is shown in Figure 29a (the crack is due to separation of the solder from the nickel plating applied for metallographic purposes). Shown in Figure 29b is the gold x-ray map. Several gold-rich areas appear near to the solder film surface. A very fine distribution of gold signal is recorded *within the solder layer*. Complete dissolution of the initial gold plating is evidenced by the gold map. However, for a much thinner solder film (Figure 30a), there is less solder volume to dissolve the gold so that its greater concentration became more apparent in the corresponding gold x-ray map (Figure 30b). Although a fine layer of gold was adjacent to the nickel plating of the Kovar, a majority of the gold is found on the solder film outer surface. This was also observed in the optical micrographs of the solder film surfaces.

***3.2.3 Electropolishing Process—Plain Kovar—*** Shown in Table 5 are the solderability parameters comparing the Diversey etched to the electropolished samples. A dramatic decrease of contact angle from $61° \pm 11°$ to $31° \pm 2°$ was recorded for A611. A decrease of 8° was observed for A260HF after electropolishing the specimens. In both cases, the improvement in contact angle was due entirely to a decrease in the interfacial tension, $\gamma_{LF}$. For the remaining fluxes, no significant changes were noted in the contact angles between the two cleaning procedures. In the instance of B1452, both $(\gamma_{SF} - \gamma_{SL})$ and $\gamma_{LF}$ decreased slightly, resulting in a small increase of $\theta_c$. A250HF and B2508 showed an increase in both $(\gamma_{SF} - \gamma_{SL})$ and $\gamma_{LF}$, leaving $\theta_c$ unchanged. For all of the fluxes, the wetting rate was improved by using the electropolishing procedure. However, no obvious trend was observed between the pairs of values of $t_W$.

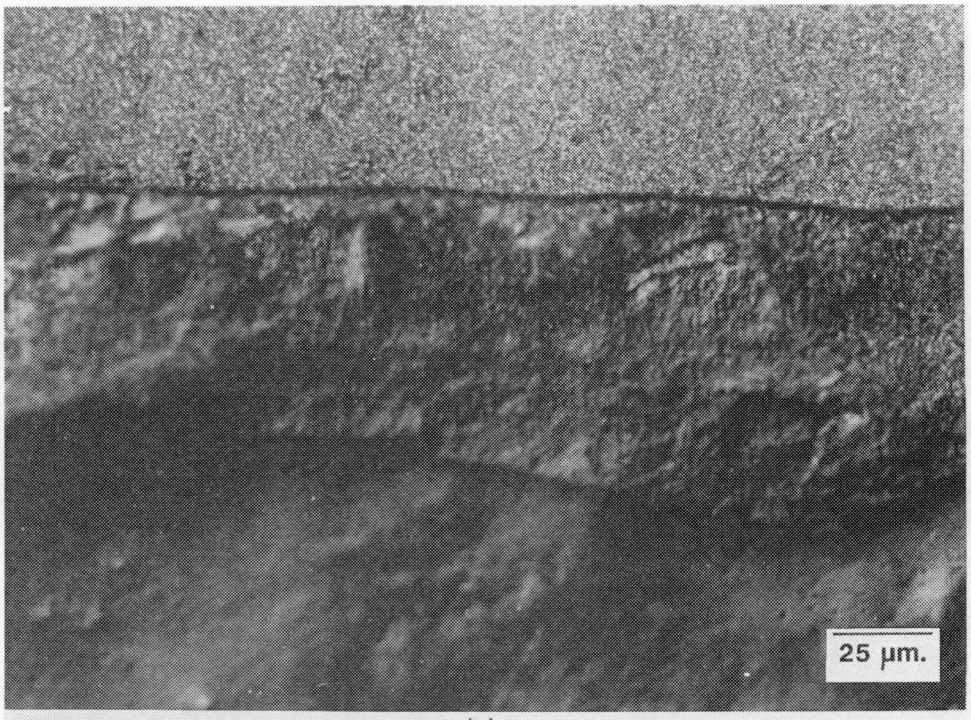


(a)

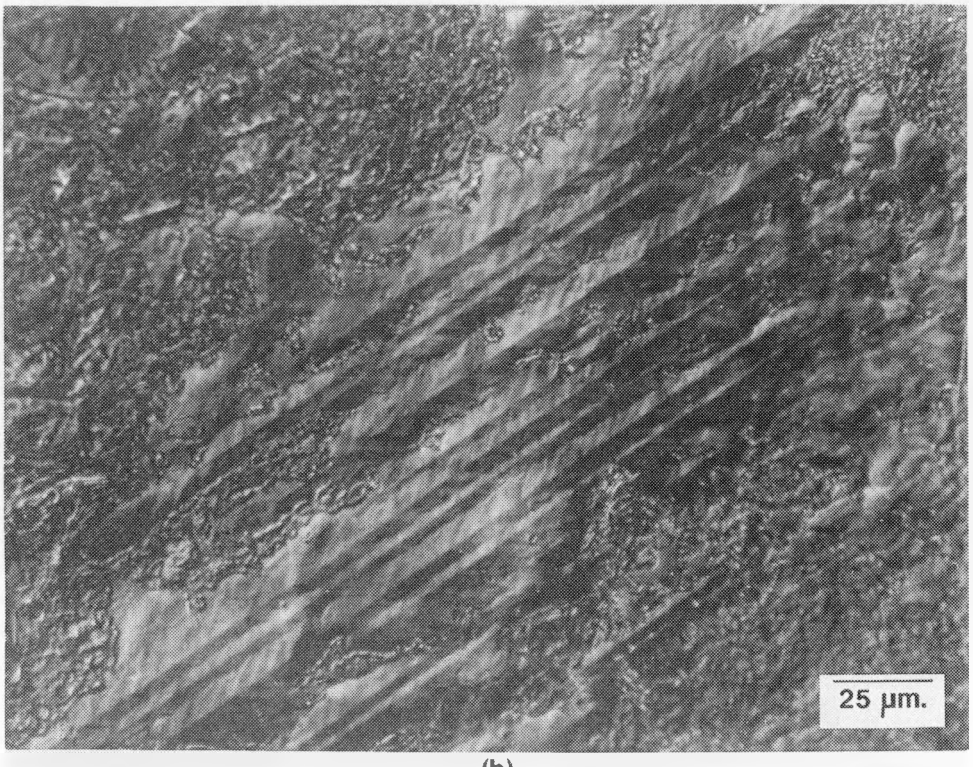


(b)

**Figure 24.** Optical micrograph (differential interference contrast) of Zone 1 from the solder film in Figure 23 (gold-nickel-plated Kovar; fluxed with A611). (a) The plated Kovar surface is at the top of the photograph. (b) Gold-tin intermetallic crystals in Zone 3 of Figure 23.


**Figure 25.** Optical micrograph (differential interference contrast) of the solder film on a gold-nickel-plated Kovar sample on which *no* flux was employed.

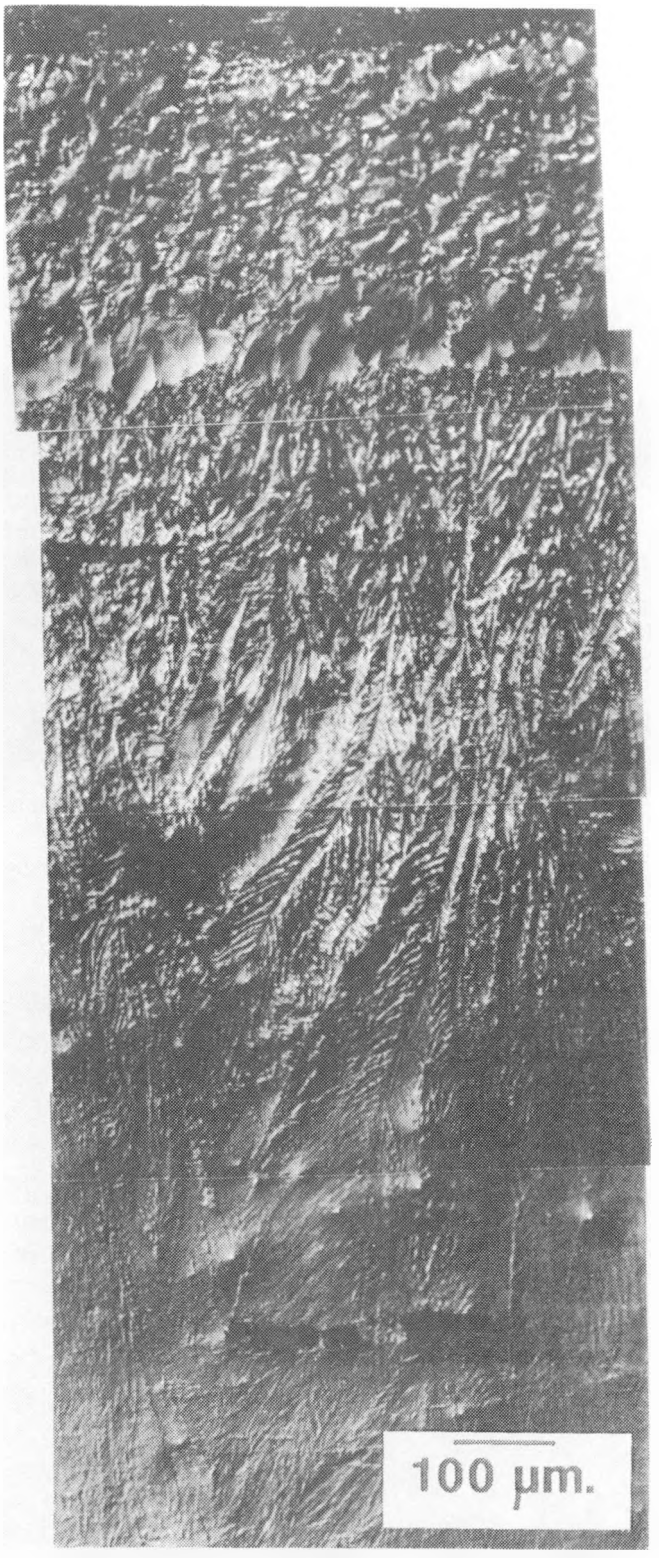


**Figure 26.** Optical micrograph (differential interference contrast) of the solder film on a gold-nickel-plated Kovar sample fluxed with B1452. The plated Kovar surface is at the top of the photograph.

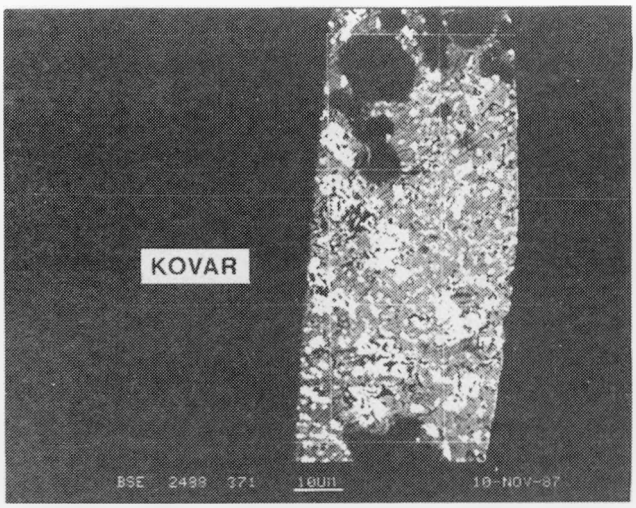


**Figure 27.** SEM micrograph (backscattered electron) of the solder-film cross section on a nickel-plated Kovar coupon fluxed with B1452. The Kovar sample (and nickel plating) are situated to the left of the image; the solder- film-free surface (which was also nickel-plated for metallography purposes) is to the right. The magnification appears below the image.

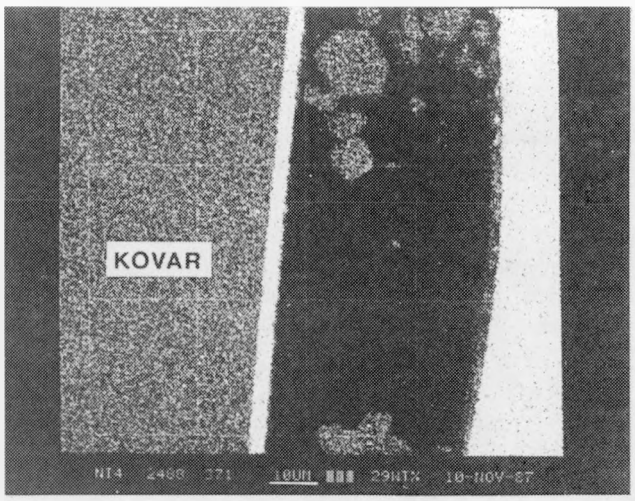


(a)

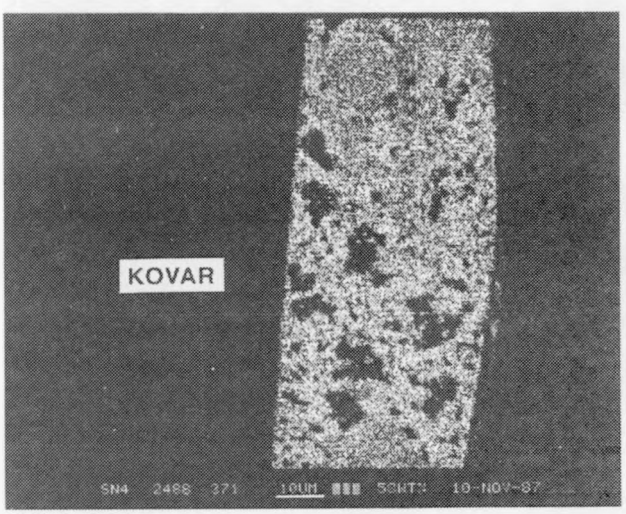


(b)

**Figure 28.** X-ray maps of the solder film at exactly the same location shown in Figure 27. The grid provides precise registration between the two images. The morphologies from left to right are: Kovar bulk; nickel plating applied to the Kovar; the solder film; and, lastly, the nickel plating on the solder-film surface (metallography). (a) *nickel* concentration, (b) *Tin* concentration.

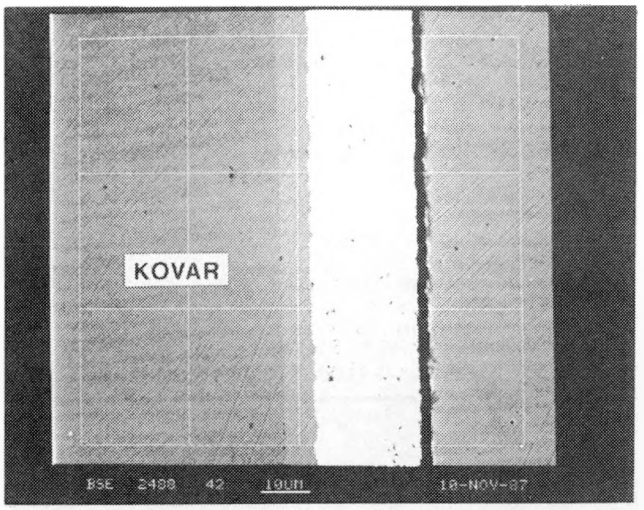


(a)

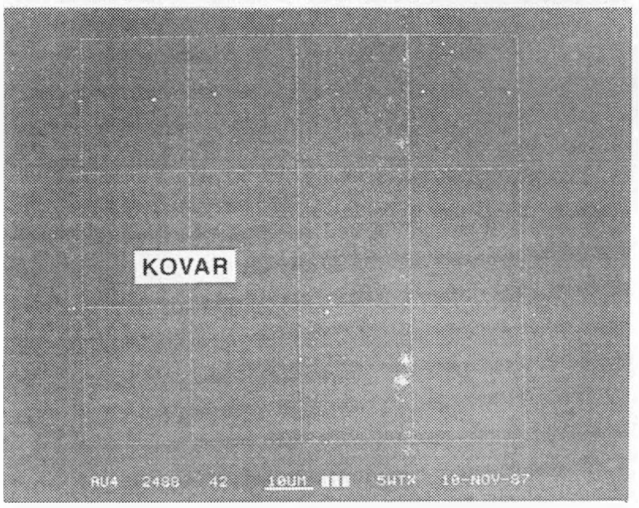


(b)

**Figure 29.** SEM micrograph (backscattered electron) of the solder-film cross section on a gold-nickel-plated Kovar coupon fluxed with A611. (a) The bulk Kovar (and nickel portion of the gold-nickel plating) is to the left of the solder film image. (b) X-ray map of *gold* concentration in (a).

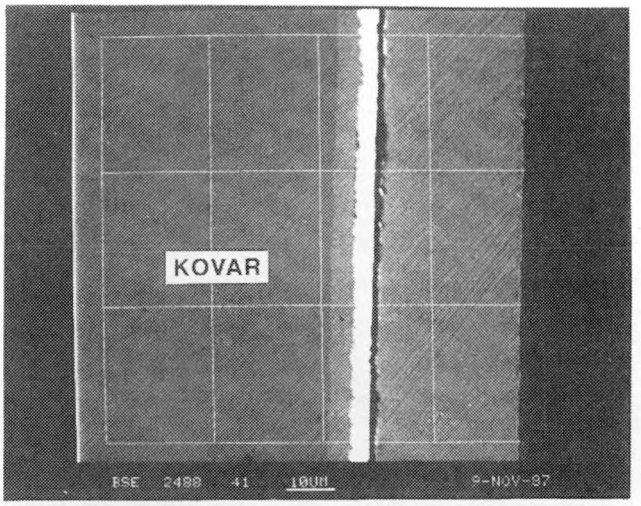


(a)

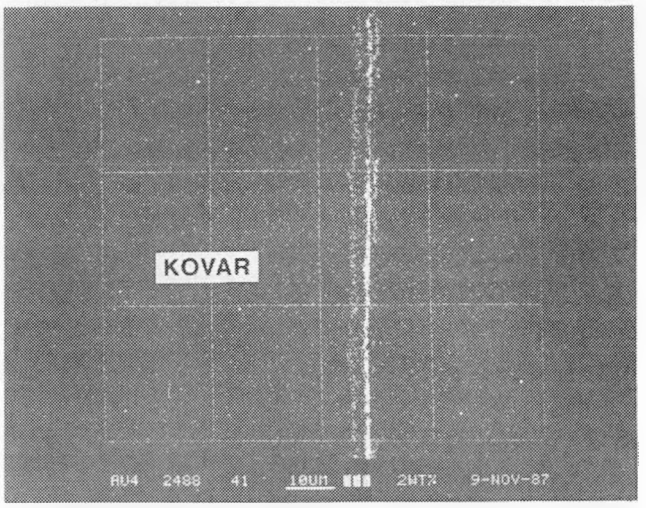


(b)

**Figure 30.** SEM micrograph (backscattered electron) of the solder-film cross section near the meniscus front (a) A gold-nickel-plated Kovar coupon fluxed with A611. (b) X-ray map of the *gold* concentration region in (a).

**Table 5. Comparison of the solderability data between the 2-min. Diversey-etching process and the 5-min electropolishing procedure on plain Kovar for each of the fluxes**

| FLUX | $\theta_c$, deg. | | $\gamma_{LF}$, dyne/cm | | $\gamma_{SF} - \gamma_{SL}$ dyne/cm | | $\dot{W}$ dyne/sec. | | $t_w$ sec. | |
|---|---|---|---|---|---|---|---|---|---|---|
| | C-ETCH | E-POLISH | C-ETCH | E-POLISH | C-ETCH | E-POLISH | C-ETCH | E-POLISH | C-ETCH | E-POLISH |
| B1452 | 29±5 | 30±5 | 430±30 | 420±30 | 380±10 | 364±7 | 1290±50 | 1530±150 | 3.2±0.2 | 3.0±0.6 |
| A260HF | 45±6 | 37±2 | 510±90 | 460±30 | 360±20 | 370±15 | 1400±100 | 1620±150 | 2.5±0.2 | 2.1±0.1 |
| B2508 | 53±5 | 53±3 | 540±80 | 740±90 | 325±15 | 450±20 | 1390±150 | 1670±100 | 2.8±0.2 | 3.1±0.2 |
| A250HF | 53±11 | 55±3 | 290±100 | 640±70 | $175^{+0}_{-30}$ | 370±15 | 600±100 | 1060±100 | 3.8±0.5 | 4.6±0.5 |
| A611 | 61±11 | 31±2 | 650±200 | 400±20 | $315^{+0}_{-40}$ | 340±10 | 1230±50 | 1390±50 | 4.7±0.3 | 3.9±0.1 |

Optical microscopy of the solder meniscuses on the electropolished sample surfaces demonstrated no influence by the Kovar surface morphology on the visual appearance of the solder film. The steep front noted on the A260HF and A250HF solder films of the Diversey-etched samples disappeared on the electropolished coupons. Although some dewetting was observed on the electropolished coupons, it was not as severe as on the chemically etched samples. No cases of nonwetting (Figures 13a and 13b) were noted for any of the fluxes applied to the electropolished specimens.

For the electropolished samples, the values of the interfacial tension, $\gamma_{LF}$, arising from use of the rosin-based flux, A611, were in close agreement with similar data recorded by Latin[16] and Howie et al.[17] In the work of Latin,[17] the author used the maximum bubble pressure method to obtain the eutectic (63Sn37Pb) solder-flux interfacial tension of 392 dyn/cm at 266°C on OFHC copper using a nonactivated, rosin-based flux (which is to be compared to the value of 400 ± 20 dyn/cm from Table 5). From the second report by Howie et al., sessile drop experiments were conducted at 400°C using lead-tin alloys that included near-eutectic compositions. The alloys were immersed in the rosin-based flux while resting on a Pyrex disk. Interfacial tension values of ~410 dyn/cm were observed. The comparison of data in Reference 17 with those in Table 4 exemplifies the similarity of the values of $\gamma_{LF}$ using different analytical techniques.

## 3.3 Flux Dilution

Throughout the previously reported results, the fluxes were used in a dilution of 1:1 by volume with isopropyl alcohol, as recommended by the flux manufacturers. The candidate flux selected for the investigation of changing the dilution was B1452. The plain Kovar samples were Diversey-etched for 2 min.

Figure 31 shows a plot of contact angle and interfacial tension, $\gamma_{LF}$, versus flux dilution. The behavior of $\theta_c$ followed closely that of $\gamma_{LF}$, with a minimum at 50% to 60% dilution. When the values of $(\gamma_{SF} - \gamma_{SL})$ were computed, very slight fluctuations were recorded that were insignificant when compared to the behavior of the contact angle. Therefore, the dependence of $\theta_c$ on flux dilution is a direct result of changes in the interfacial tension between the flux and liquid solder. Finally, the wetting rate and time to maximum meniscus weight showed no significant dependence on flux dilution.

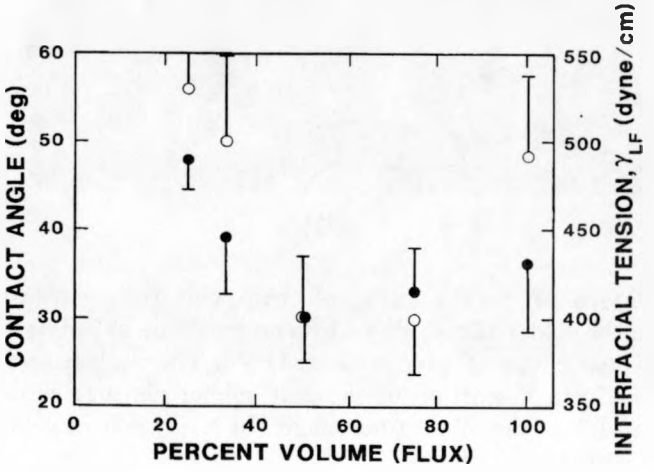


**Figure 31.** Dependence of $\theta_c$ and $\gamma_{LF}$ on the strength of dilution of B1452 with isopropyl alcohol. The plain Kovar samples were Diversey-etched for 2 min prior to tinning. Solder temperature was 260°C. The solid circles refer to the contact angle data, and the open circles to the interfacial tension results.

## 3.4 Effect of Solder Temperature

Figure 32 shows the dependence of the contact angle on the solder temperature for the two fluxes, A611 and B1452, used on plain Kovar cleaned by electropolishing. For the B1452 flux, a slight decrease in the contact angle with increasing temperature, $-0.08°/°C$, was recorded by linear-least-squares analysis. The correlation was weak, with an $R^2$ value of 0.74. No significant trend was statistically confirmed for the A611 flux ($R^2=0.27$). Examples of the wetting curves for both A611 and B1452 for solder temperatures of 215°C and 245°C are shown in Figure 33. While the equilibrium contact angles changed very little, the curves showed dramatic differences in the wetting rate and time to maximum wetting force. The solderability parameters are outlined in Table 6. For the case of A611, the increased solder pot temperature resulted in an increased wetting rate and a corresponding decrease in time to maximum meniscus weight. For B1452, no significant trend can be associated between the temperature and the wetting rate. However, a slight decrease in $t_W$ with increasing temperature corresponded to a diminished negative meniscus weight observed at the start of the lower-temperature wetting curves.

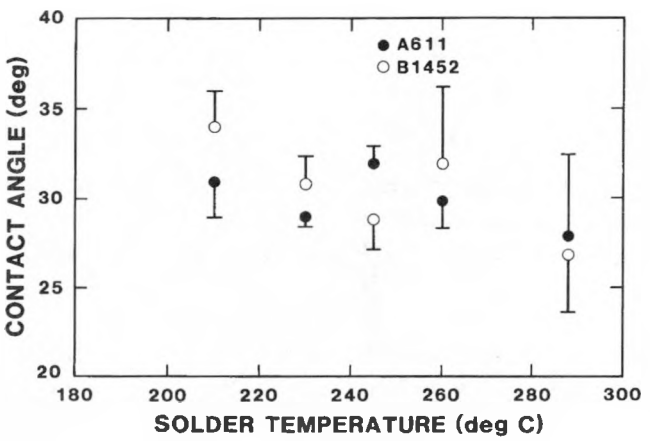


**Figure 32.** Dependence of the contact angle, $\theta_c$, on the solder temperature with the use of two fluxes: A611 (solid circles) and B1452 (open circles). The samples received the electropolishing treatment.

The values of $\gamma_{LF}$ and $(\gamma_{SF} - \gamma_{SL})$ as a function of solder temperature (Table 6) were generally the same in the temperature range of 215°C to 260°C for the A611 flux. The drop in $(\gamma_{SF} - \gamma_{SL})$ and $\gamma_{LF}$ at 288°C caused a slight decrease in $\theta_c$. However, the drop in $\theta_c$ with increasing solder temperature for B1452 was the result of a generally observed increase in $(\gamma_{SF} - \gamma_{SL})$; the changing values of $\gamma_{LF}$ did not contribute to the trend of $\theta_c$.

Finally, qualitative observations of the solder films showed that the degree of porosity noted with the use of B1452 increased as the temperature was raised, and so did the magnitude of the flux residues; this final observation also applied to the use of A611. As the temperature was increased, the difficulty of removing flux residue also increased.

## 3.5 T-Peel Strength Measurements

The T-peel strengths of the coupons cleaned by the Diversey surface etch and coated with one of the five fluxes are shown in Table 7, together with the contact angles determined by solderability testing. The error is $1\sigma$ of four samples. The data from the gold-nickel-plated coupons and the T-peel strengths of the plain Kovar samples that had been electro-polished are listed. The strength did not correlate well with the contact angle measurements as determined by linear-least-squares analysis ($R^2 = 0.58$).

From a visual examination of the T-peel fracture surfaces, we observed a mixture of fracture paths that consisted of failure at both the Kovar-solder interface and the copper-solder interface. When the percent of failure at the Kovar-solder interface was reviewed as a function of T-peel strength, an inverse relationship was observed (Table 8). Comparing the data from electropolished Kovar samples with data from chemically etched samples, both having been coated with A611, we see that the percent of failure at the Kovar-solder interface dropped from 80% to 35% after switching from the chemical etch to the electropolish. The corresponding peel strength improved from $7\times 10^6$ to $9.4 \times 10^6$ dyn/cm.

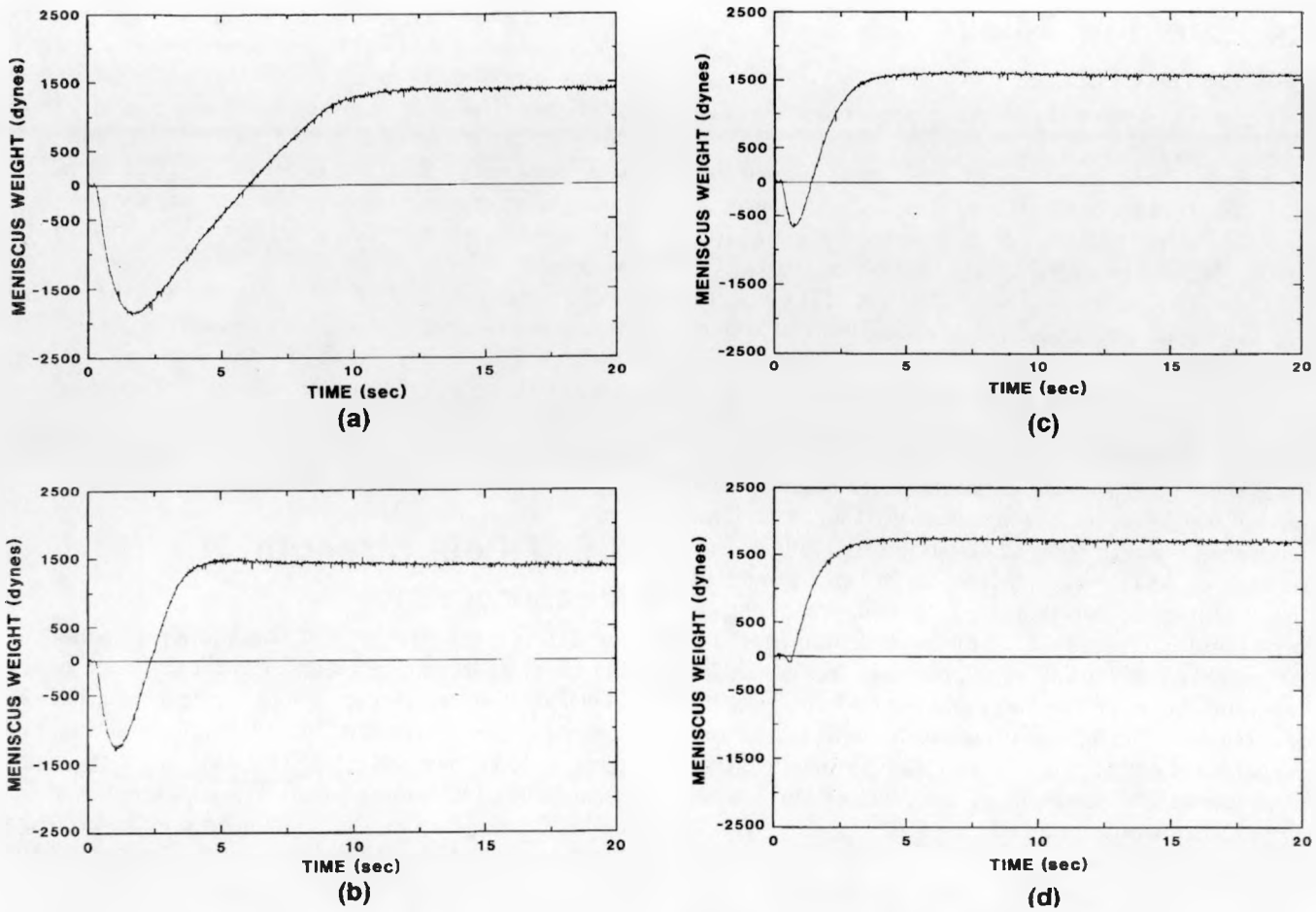


**Figure 33.** Representative wetting curves of the electropolished, plain Kovar samples fluxed with either A611 of B1452 and tested with solder temperatures of 215°C and 245°C; (a) A611, 215°C, (b) A611, 245°C, (c) B1452, 215°C, and (d) B1452, 245°C.

The solder fracture surface appeared as a rough, dull gray with the gray hue slightly darker on the copper coupon than on the Kovar. Figure 34 shows SEM micrographs of the fracture morphology representing the sample that was Diversey-etched and fluxed with A611. Figure 34a corresponds to surface "A" and 34b to surface "B" of the schematic in Figure 34c. The fracture morphology in Figures 34a and 34b is a mixture of brittle facets and ductile rupture. The brittle features were due to the formation of copper-tin intermetallic crystals; the large-scale deformation of the surface arises from the ductile solder layer. The morphology in Figure 34 covered ~20% of the failed surface. The remaining surface arose from failure along the Kovar-solder interface, the SEM micrographs of which are shown in Figures 35a and 35b. Figure 35a is the Kovar side and 35b is the complementary solder film surface. Figure 35a shows that some of the solder remained attached to the Kovar. However, the solder film was intermittent because the grain boundary etching of the Kovar by the Diversey is clearly evident in the center of the photograph. Failure between the Kovar and the more ductile lead-rich phase is evident in Figure 35a; the remaining features resulted from separation by the tin-rich phase. It was possible to distinguish between the two phases by means of low-magnification observations in which an "imprint" of the "butterfly" structure (characteristic of the lead-rich phase) was left on the Kovar surface. The mating surface on the solder film, Figure 35b, showed the relatively smooth surface expected of easy separation from the Kovar in the absence of adhesion. A similar series of SEM micrographs were taken of the fracture surface of the sample that had been Diversey-cleaned and fluxed with B1452. In this case, the fracture path was farther away from the copper-solder interface and showed a slightly greater degree of ductility on both complementary surfaces when compared to the results in Figure 35.

Table 6. Solderability data as a function of solder temperature for the two fluxes, A611 and B1452

| FLUX | T deg. C | $\gamma_{LF}$ dyne/cm | $\gamma_{SF} - \gamma_{SL}$ dyne/cm | $\dot{W}$ dyne/sec | $t_w$ sec |
|---|---|---|---|---|---|
| A611 | 215 | 380±20 | 320±10 | 460±100 | 11±1 |
| | 230 | 390±10 | 340±10 | 1000±30 | 5.7±0.2 |
| | 245 | 390±15 | 330±10 | 1230±100 | 4.1±0.3 |
| | 260 | 390±15 | 340±10 | 1390±50 | 3.9±0.1 |
| | 288 | 310±40 | 270±20 | 1490±200 | 3.3±0.2 |
| B1452 | 215 | 450±20 | 370±10 | 1310±50 | 3.9±0.2 |
| | 230 | 460±20 | 390±15 | 1540±50 | 4.1±0.2 |
| | 245 | 450±30 | 390±20 | 1390±100 | 3.6±0.5 |
| | 260 | 420±30 | 360±20 | 1310±50 | 3.2±0.2 |
| | 288 | 460±20 | 410±10 | 1340±50 | 3.1±0.3 |

Table 7. Comparison between the T-peel strength and solderability contact angle

| FLUX | $\theta_c$ deg | T-PEEL STRENGTH x $10^6$ dyne/cm |
|---|---|---|
| | PLAIN KOVAR, CHEMICALLY ETCHED | |
| B1452 | 29 ± 5 | 11.0 ± 0.5 |
| A260HF | 45 ± 6 | 10.0 ± 0.7 |
| B2508 | 53 ± 5 | 10.2 ± 0.5 |
| A250HF | 53 ± 11 | 9.5 ± 0.4 |
| A611 | 61 ± 11 | 7 ± 2 |
| | PLAIN KOVAR, ELECTROPOLISHED | |
| A611 | 31 ± 2 | 9.4 ± 0.5 |
| | GOLD-NICKEL PLATED KOVAR | |
| A611 | 11 ± 5 | 10.4 ± 0.2 |

**Table 8. Comparison between T-peel strength and the crack propagation path for the plain Kovar-OFHC copper pull samples**

| FLUX | % OF FAILURE AT KOVAR-SOLDER INTERFACE | T-PEEL STRENGTH x $10^6$ dyne/cm | CONTACT ANGLE deg |
|---|---|---|---|
| A611 | 80 ± 5 | 7 ± 2 | 61 ± 11 |
| A250HF | 35 ± 5 | 9.5 ± 0.4 | 53 ± 11 |
| A260HF | 15 ± 5 | 10.0 ± 0.7 | 45 ± 6 |
| B1452 | 10 ± 5 | 11.0 ± 0.5 | 29 ± 5 |
| B2508 | 7 ± 5 | 10.2 ± 0.5 | 53 ± 5 |

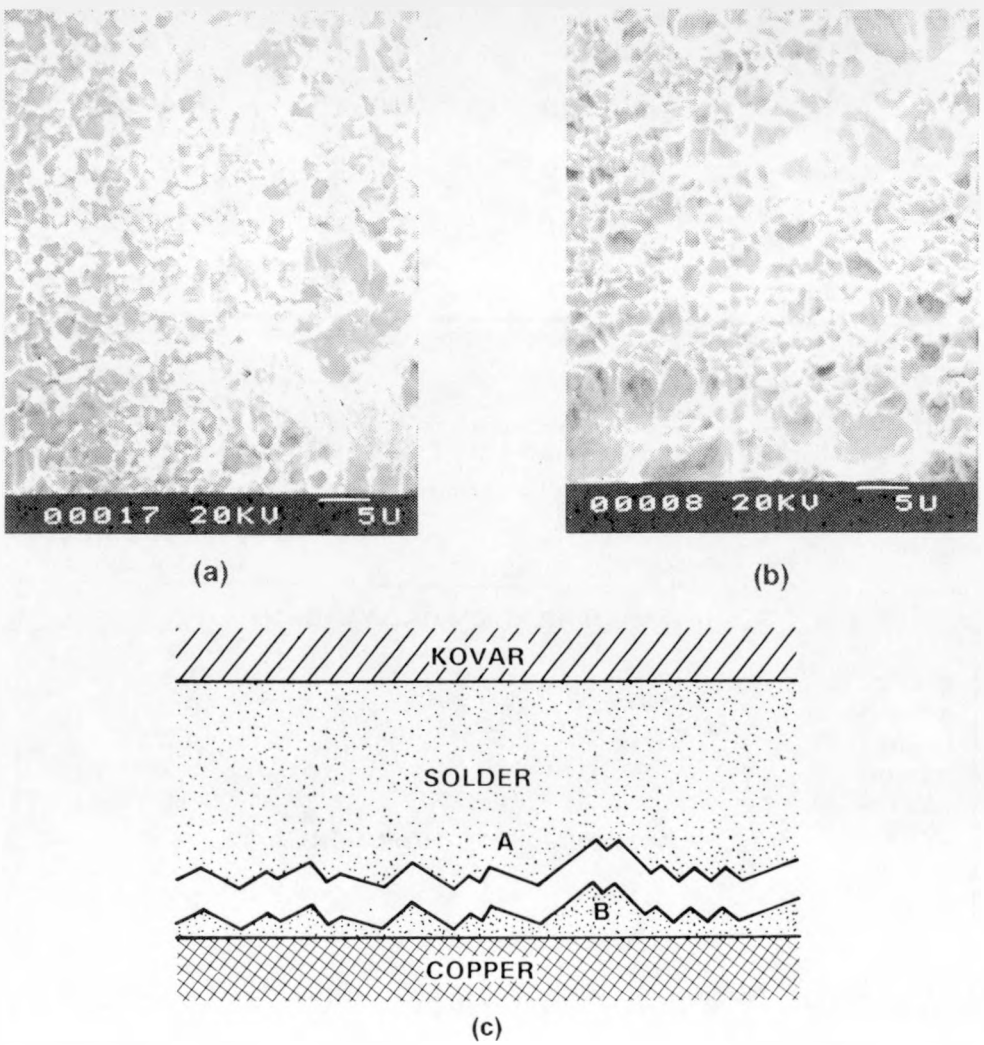


**Figure 34.** SEM micrograph (secondary electron) of the T-peel fracture surfaces from a Diversey-etched, plain Kovar specimen fluxed with A611 in which failure took place near the copper-solder interface. (a) The surface adjacent to the solder film, (b) the surface on the copper side, and (c) schematic of the fracture path.

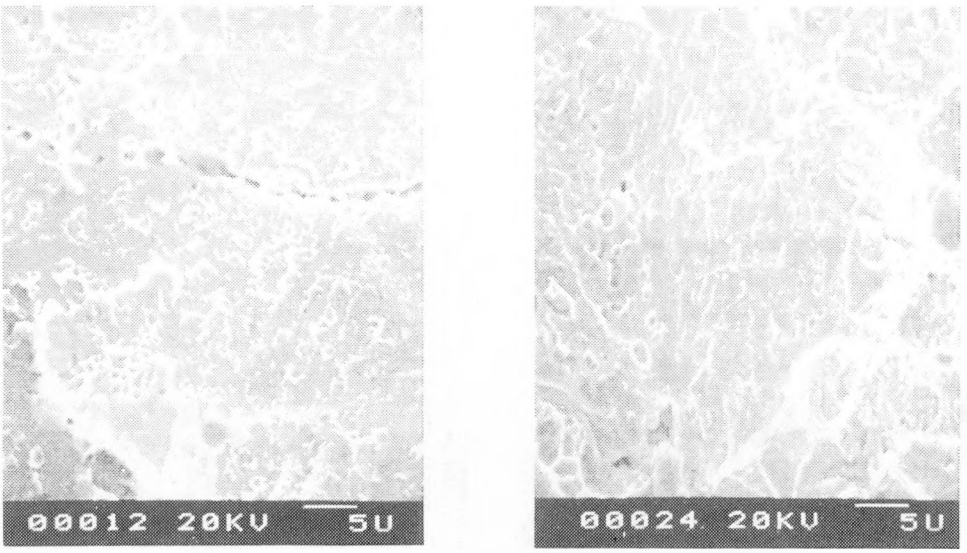


**Figure 35.** SEM micrographs (secondary electron) of the T-peel fracture surfaces on the Diversey-etched, plain Kovar sample fluxed with A611. The fracture path was along the solder-Kovar interface, (a) The Kovar surface, and (b) the solder film surface.

Flux entrapment, indicated by the presence of voids, was observed to some degree on all samples. The distribution of such pores differed between A611, which had very few and rather small (~0.008 cm in diameter) voids, and all of the organic-acid fluxes, in which the void size and number were generally greater (Figure 36). However, the data in Table 9 showed no dependence between the peel strength and the amount of voids for these samples.

The last case to be examined qualitatively is the gold-nickel-plated coupon. For some samples, the bond could not be fractured; the copper leg to which the grip was attached failed before the joint began to tear. Therefore, the average peel strength in Table 7 includes only samples showing a failure along the joint. The fracture surface appeared similar to those of the previously discussed samples.

# 4. Discussion

## 4.1 Parameters Controlling the Contact Angle

The wetting behavior of 60Sn40Pb solder on Kovar was quantitatively described by the contact angle, $\theta_c$. The smaller the value of $\theta_c$, the better the wettability or solderability. The flux decreases the value of $\theta_c$ by two processes: (1) by creating and protecting the freshly cleaned and deoxidized surface, and (2) by lowering the solder-flux interfacial tension. With regard to the parameters in Young's equation, mechanism (1) gives rise to a larger value of ($\gamma_{SF} - \gamma_{SL}$) by increasing $\gamma_{SF}$. It is assumed that the value of $\gamma_{SL}$ is constant where the solder has wet the substrate irrespective of the prior condition of the substrate, since the surface contamination is displaced by the advancing liquid alloy. Intrinsically, the effectiveness of each flux to increase ($\gamma_{SF} - \gamma_{SL}$) and decrease $\gamma_{LF}$ depends on the specific chemicals contained in the material (which includes wetting agents as well as the corrosive) and on the dilution of the flux. The extrinsic factors affecting $\theta_c$ include the operating temperatures and the condition of the substrate surface at the time of soldering.

In much of the data, the solder-flux interfacial tension, $\gamma_{LF}$, played a significant role in the behavior of $\theta_c$. This observation is not unexpected when comparing data between the different fluxes (Table 2). On the other hand, Table 5 illustrates tests in which the same flux was applied to differently cleaned surfaces. The result was significant changes in $\gamma_{LF}$, the characteristics of which were very dependent on the particular flux in use.

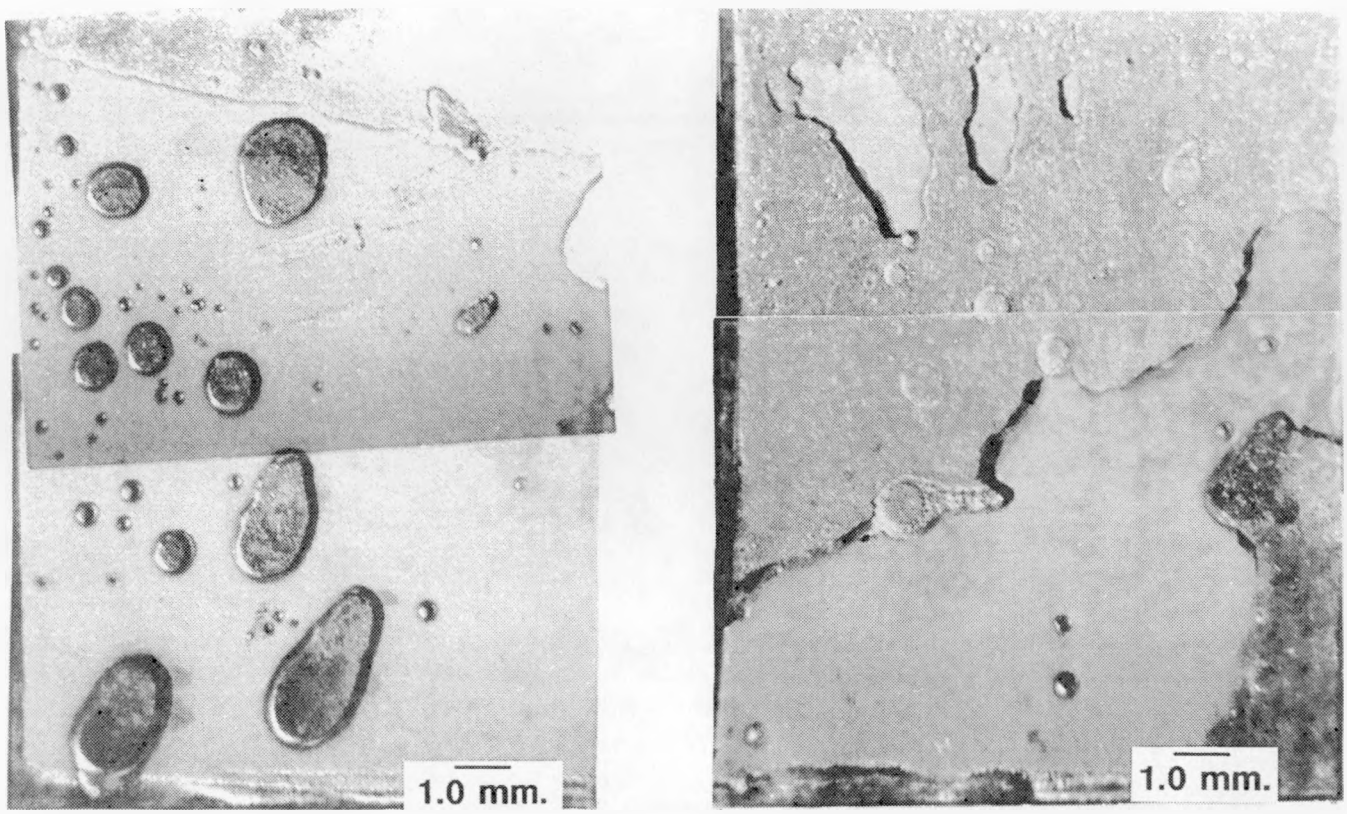


**Figure 36.** Optical micrographs (bright field) of T-peel fracture surfaces (a) Diversey-etched, plain Kovar fluxed with B2508, and (b) Diversey-etched, plain Kovar fluxed with A611. In both cases, the Kovar leg of the joint is being viewed.

**Table 9. Comparison between the T-peel strength and the area fraction of voids on the fracture surface**

| FLUX/SAMPLE | AREA FRACTION OF VOIDS | T-PEEL STRENGTH x $10^6$ dyne/cm |
|---|---|---|
| A611/1-4, F | 0.045 | 5.6 |
| A611/1-1, F | 0.034 | 6.7 |
| B2508/A-1 | 0.103 | 9.6 |
| B2508/A-3 | 0.074 | 10.5 |
| B1452/G | 0.047 | 9.5 |

The dependence of $\gamma_{LF}$ on the substrate surface condition is based on the by-products generated through the corrosive action of the flux as it cleans the surface. The reaction products, which are carried away by the flux, may favorably segregate to the solder-flux interface if the result is a decrease in the system's free energy. It has been observed experimentally[18,19] that the interfacial tension between two liquids can be extremely sensitive to such surface active contaminants present in either material. On the other hand, surface inactive solutes, by remaining dissolved in one of the liquids, may change the bulk properties of the phase enough to also affect the interfacial tension. This hypothesis has some bearing on the results of this study.

Under high-magnification, bright-field optical microscopy, the plain Kovar surface had a slightly brighter appearance after electropolishing than after chemical etching, when the differences in surface roughness are taken into account. Therefore, the chemically etched surface appeared to have more surface contamination. Examining the data for flux A611 in Table 5, we found that the value of $(\gamma_{SF} - \gamma_{SL})$ increased only slightly from chemical etching to electropolishing. This observation suggests that the flux could achieve nearly the same surface conditions after either cleaning treatment. Therefore, the greater quantity of reaction by-products generated from the chemically cleaned samples and dissolved in the flux coating were responsible for the larger values of $\gamma_{LF}$.

A similar relationship between the interfacial tension, $\gamma_{LF}$, and the substrate surface condition was observed in the data of Mayhew and Wicks.[4] Although the substrates were copper, the effect of surface condition on $\gamma_{LF}$ is clearly demonstrated. Shown in Table 10 are the values of $\theta_c$ and $\gamma_{LF}$ taken from the reference. $(\gamma_{SF} - \gamma_{SL})$ was calculated by the present authors. For these experiments, the solder was 63Sn37Pb at 260°C. The flux was water, white-rosin-based with either 0.05%, 0.50%, or 1.00% activator. The surface oxidation of the copper samples increased in the sequence of A, B, C, and D. For the activator levels of 0.50% and 1.00%, as the degree of surface contamination increased, the value of $\gamma_{LF}$ increased, while $(\gamma_{SF} - \gamma_{SL})$ was constant. This is the same trend observed between the chemically etched and the electropolished data for flux A611 and A260HF.

**Table 10. Analysis of the data in Reference 4 that compare the values of the solderability parameters as a function of the activation level of the flux and the surface oxidation of the substrates**

| SUBSTRATE SAMPLE | 0.05 | | | 0.5 | | | 1.0 | | |
|---|---|---|---|---|---|---|---|---|---|
| | $\theta_c$ | $\gamma_{LF}$ | $\gamma_{SF}$-$\gamma_{SL}$ | $\theta_c$ | $\gamma_{LF}$ | $\gamma_{SF}$-$\gamma_{SL}$ | $\theta_c$ | $\gamma_{LF}$ | $\gamma_{SF}$-$\gamma_{SL}$ |
| A | 17 | 417 | 398.8 | 11.5 | 376 | 368 | 10 | 368 | 362 |
| B | 38 | 482 | 380 | 19 | 394 | 372 | 18 | 386 | 367 |
| C | — | — | — | 23 | 413 | 380 | 22.5 | 394 | 364 |
| D | — | — | — | 25.5 | 416 | 375 | 28 | 423 | 373 |

Data after —
A. Mayhew and G.R. Wicks Proc. Inter. NEPCON III (1971) p. 45
A — degreased and chemically cleaned
B, C, and D, likewise cleaned, then oxidized by incr. amounts (time) in air, 150°C.
Flux — water white resin - w/given % activator.
Substrates were copper.

For flux B1452, no significant change was recorded for the values of $\gamma_{LF}$ and $(\gamma_{SF} - \gamma_{SL})$ between the two cleaning processes. Therefore, the solder-flux interfacial tension was not sensitive to by-products contained in the flux layers arising from these two test series. A comparison of $\gamma_{LF}$ and $(\gamma_{SF} - \gamma_{SL})$ between cleaning procedures for the other two fluxes, A250HF and B2508, was slightly more ambiguous. In both cases, significant increases in $\gamma_{LF}$ and $(\gamma_{SF} - \gamma_{SL})$ were observed, while $\theta_c$ remained unchanged (Table 5). The increase in $(\gamma_{SF} - \gamma_{SL})$ indicates that the cleaning capabilities of fluxes A250HF and B2508 were sensitive to the different surface conditions left by the two cleaning procedures.

Very little change in $\gamma_{LF}$ and $(\gamma_{SF} - \gamma_{SL})$ was noted for flux B1452 between the two cleaning procedures. However, increasing the chemical etching time before using the B1452 flux from 0.5 to 2.0 min lowered the value of $\gamma_{LF}$. We hypothesize that, as the cleaning process became more effective at removing surface contaminants with longer cleaning times, the value of $\gamma_{LF}$ decreased as fewer corrosion products were entrapped in the flux film. This behavior was not observed between the 2-min etched samples and the electropolished samples because for the flux B1452, the *difference* in degree of surface contamination was probably not enough to change the two values of $\gamma_{LF}$.

## 4.2 Effect of Surface Plating on Solderability

The presence of surface plating had a pronounced effect on the interfacial tensions. The gold plating was almost completely dissolved by the solder so that (effectively) the liquid alloy was wetting the nickel underlayer, and the values of $\gamma_{SL}$ would be comparable. Therefore, the values of $\gamma_{SF}$ were also similar for the gold-nickel- and nickel-plated coupons since the quantity, $(\gamma_{SF} - \gamma_{SL})$, was identical at a given flux. These data are summarized in Table 11. For a given plating layer, a larger disparity existed between the values of $(\gamma_{SF} - \gamma_{SL})$ calculated for the B1452 and A611 fluxes as opposed to a similar comparison between the same fluxes applied to the plain Kovar surface. This suggests that the plated surfaces were more sensitive to the different fluxes than were the electropolished Kovar surfaces.

The change of $\gamma_{LF}$ when the gold-nickel and nickel platings were added to the Kovar was very sensitive to the flux in use. For both platings, the value of $\gamma_{LF}$ caused by the flux A611 was lower, and that from the use of B1452 flux, higher, than the respective values for plain Kovar. The lower contact angles for the gold-nickel-plated samples were caused by slightly lower $\gamma_{LF}$ as compared to the nickel-plated samples. The segregation of the gold component to the solder film surface (Figure 30b) contributed to the drop in $\gamma_{LF}$.

With the use of the A611 flux, the lower contact angles achieved with either plating were predominantly the result of a lower value of $\gamma_{LF}$ as compared to the electropolished coupons. However, when the flux B1452 was used, the lower contact angles were largely caused by the higher values of $(\gamma_{SF} - \gamma_{SL})$ as compared to the case of the plain Kovar surface. We conclude that the B1452 flux achieved a larger difference of $(\gamma_{SF} - \gamma_{SL})$ on the plated surfaces than on those that were electropolished.

**Table 11. Comparison of the solderability parameters of the plated samples and the electropolished coupons as a function of the flux**

| E-POLISH | | | GOLD-NICKEL-PLATED | | | NICKEL-PLATED | | |
|---|---|---|---|---|---|---|---|---|
| $\theta_c$ | $\gamma_{LF}$ | $(\gamma_{SF} - \gamma_{SL})$ | $\theta_c$ | $\gamma_{LF}$ | $(\gamma_{SF} - \gamma_{SL})$ | $\theta_c$ | $\gamma_{LF}$ | $(\gamma_{SF} - \gamma_{SL})$ |
| | | | | A611 | | | | |
| 31 | 400 | 340 | 11 | 360 | 350 | 24 | 380 | 350 |
| | | | | B1452 | | | | |
| 30 | 420 | 364 | 15 | 460 | 440 | 24 | 480 | 440 |

## 4.3 Effect of the Flux Dilution

In Figure 31, the contact angle as a function of the dilution of the B1452 flux was minimal at a concentration of ~50% to 60%. The similar dependence on dilution strength demonstrated by $\gamma_{LF}$ was responsible for the overall trend of $\theta_c$. The values of $\theta_c$ were not sensitive to $(\gamma_{SF} - \gamma_{SL})$. It is suggested that the dilution dependence of $\gamma_{LF}$ was caused by the simultaneous occurrence of two phenomena; one causing $\gamma_{LF}$ to decrease with increasing flux concentration below 50% to 60% dilution, and the other increasing the value of $\gamma_{LF}$ as the proportion of flux increased at concentrations >60%. The decrease of $\gamma_{LF}$ as the flux concentration increased between 0% and 60% was caused by a transition from the solder *surface* tension (510 dyn-cm$^{-1}$)[20] to the solder-flux *interfacial* tension (of ~430 dyn-cm$^{-1}$). The slight increase of $\gamma_{LF}$ beyond 60% resulted from an increased concentration of reaction by-products created by the greater corrosive action of the dilution.

## 4.4 Effect of Solder Temperature

The solder temperature affects the wetting behavior through two factors; first, by the equilibrium conditions as determined by $\gamma_{LF}$ and $(\gamma_{SF} - \gamma_{SL})$, and secondly by the kinetics of wetting as described extrinsically by $\dot{W}$ and $t_W$.

For flux A611, no significant change was observed in either $\gamma_{LF}$ or $(\gamma_{SF} - \gamma_{SL})$ over the temperature range 215°C to 260°C (Table 6). The decrease in $\theta_c$ at 288°C was caused by a drop in $\gamma_{LF}$. A decrease of $(\gamma_{SF} - \gamma_{SL})$ between 260°C and 288°C is evidence that the fluxes' chemical activity had diminished slightly. The decrease of $(\gamma_{SF} - \gamma_{SL})$ was not the result of increased oxidation of the Kovar surface since the value of $\gamma_{LF}$ would have increased with the greater volume of reaction by-products. Rather, the decrease of $(\gamma_{SF} - \gamma_{SL})$ and $\gamma_{LF}$ was due to a temperature-sensitive change in the flux. Therefore, the temperature in the range 215°C to 260°C did not measurably affect the thermodynamic equilibrium of the solder-flux-substrate system.

For the case of B1452, the contact angle decreased slightly with increasing temperature. This trend was caused by a nonmonotonic increase in $(\gamma_{SF} - \gamma_{SL})$; no overall trend appeared to exist for the values of $\gamma_{LF}$. Therefore, the increasing temperature improved the equilibrium conditions of wetting by larger values of $(\gamma_{SF} - \gamma_{SL})$ that can be qualitatively explained by a cleaner substrate surface as the result of improved chemical activity of the flux.

As for the effect of temperature on wetting kinetics of the A611 flux as measured by $\dot{W}$ and $t_W$, an increase in $\dot{W}$ and decrease in $t_W$ with increasing temperature was observed. Therefore, increasing the solder temperature by using A611 increased the speed in which the flux reached a level of chemical activity that was constant in the temperature range 215°C to 260°C. This was indicated by the relatively constant values of $(\gamma_{SF} - \gamma_{SL})$ and $\gamma_{LF}$.

For flux B1452, the overall increase in chemical strength with temperature was not accompanied by an increase in the wetting rate. However, the value of $t_W$ noticeably decreased on raising the temperature and can be explained by a decrease of the negative meniscus weight portion of the wetting curve (Figure 33). Therefore, $t_W$ was a more sensitive indicator of the speed of wetting than was $\dot{W}$ for the range of testing temperatures.

To summarize, the temperature did not alter the solder-flux-substrate equilibrium of A611 between 215°C and 260°C. However, the higher temperatures did decrease the time for the system to reach equilibrium. For B1452, increased temperatures slightly improved the thermodynamics through the value of $(\gamma_{SF} - \gamma_{SL})$; $\gamma_{LF}$ remained generally unchanged. The improved kinetics of the wetting process were reflected in $t_W$ more so than in the wetting rate. Therefore, the optimum operating temperature for the A611 flux (diluted) was 260°C. Similarly, the B1452 flux demonstrated optimal solderability parameters at 260°C to 288°C. However, for both fluxes, the amount and tenacity of flux residues increased with temperature.

An analysis was made as to the possible effect of the time-dependent temperature profile of the immersed coupon on the wetting rate. Hypothetically, if the temperature gradient along the coupon was the controlling parameter for the rate of meniscus rise, then the meniscus rise should be extremely rapid. The reason is that the coupon temperature at an infinitely small distance ahead of the solder front would be nearly the same temperature as that of the solder. The time lag resulting from heating the Kovar substrate just ahead of the solder was calculated to be negligibly small. Therefore, if the temperature controlled the rate of meniscus rise, then the solder should have risen very quickly and shown similar behavior for the different fluxes.

This scenario was not observed in the present data. First, at similar temperatures, the wetting rates (and $t_W$) were quite different between the two fluxes. Secondly, the dependencies of $\dot{W}$ and $t_W$ on temperature were not the same for the two fluxes. We conclude that the temperature dependencies of $\dot{W}$ and $t_W$ were reflected primarily in the chemical kinetics of

the individual fluxes and not explicitly by the time-temperature profile of the Kovar coupons.

## 4.5 T-Peel Data Analysis

The data in Table 7 show that the T-peel test results did not precisely follow the trend recorded for the contact angles. Linear-least-squares fits made between the data of S (the T-peel strength) and the solderability parameters $\theta_c$, $\gamma_{LF}$, and $(\gamma_{SF} - \gamma_{SL})$ of Table 2 showed very poor correlation values ($R^2$) of 0.58, 0.29, and 0.06, respectively. This observation was not entirely unexpected because of the complexity associated with the mechanical behavior of a joint composed of two different substrates. The data summarized in Table 8 showed an increase in T-peel strength corresponding to an increasing amount of failure at the copper-solder interface. As the Kovar-solder bond strength increased to that of the copper-solder interface, a larger percentage of failure took place at the copper-solder layer until the strength of the Kovar-solder interface exceeded that of the copper; and nearly all of the failure took place at the latter region. The copper-solder bond strength can be approximated from the failure of the T-peel sample that was fluxed with B2508, since nearly the entire failure took place at the copper-solder interface; that value was $10.2 \times 10^6$ dyn-cm$^{-1}$. Therefore, although it was not possible to compute the numerical strength of the Kovar-solder joints because of the mixed-mode failure, a qualitative assessment of the fracture morphology suggests that the flux does affect the intrinsic mechanical strength of the joint.

## 4.6 Mercury Switch Leads—Direct Evaluation of Solderability

We tried to determine whether the contact angle formed by the 60Sn40Pb solder that was allowed to wet the actual mercury switch lead wire could be measured using the meniscometer and the wetting balance. The leads from switches processed at Fifth Dimension, Inc. were removed from the assemblies and subjected to the same Diversey cleaning process as the Kovar coupons. The wires had a diameter of 0.025 cm. Although the meniscometer measurements were successful in measuring the meniscus rise, the meniscus weight tests (on the wetting balance) were inconclusive because the extremely small meniscus generated a signal from the microbalance that was within the electrical noise. Nevertheless, visual observations of the wires by optical microscopy revealed some interesting results. Among the switch assemblies delivered for testing were those having a light-gray metallic surface finish and others showing a dull, slightly greenish tint. Attempts by engineers at Fifth Dimension to tin the discolored leads failed; but a 10-$\mu$m, uniformly distributed solder film did cover the wires with the light-gray, metallic surface when tested at SNL, Albuquerque. To determine the difference in wetting behavior (and surface appearance) between the two "groups" of samples required an Auger analysis on one assembly from each of the two groups.[21]

A summary of those results indicated that the discolored switches were covered with an organic film estimated at >300 nm and consisting chiefly of carbon and oxygen. The assemblies with the light-gray surface shows only the expected elemental constituents of Kovar: primarily iron, nickel, and cobalt. The presence of organic films on the surface is quite enough to inhibit the cleaning action of the Diversey etchant as well as the flux, thereby preventing the solder from wetting the wire. These experimental results clearly explain the inconsistent tinning of the Kovar leads on the mercury switch. The improved cleaning capability of the electropolish treatment was capable of providing a solderable surface regardless of the variable condition of the as-received Kovar leads.

## 4.7 Status—Switch #371925

Currently, the electropolishing process developed as part of this study is being employed as the precleaning treatment for the Kovar leads of the switch #371925 before tinning with the 60Sn40Pb solder alloy. In the tinning operation, the A611 flux (diluted 1:1 by volume with isopropyl alcohol) is now capable of promoting the excellent wetting properties demonstrated in the laboratory experiments.

# 5. Summary and Conclusions

Solderability testing, as quantified by the contact angle formed between the substrate and the liquid solder, was performed on Kovar coupons immersed into 60Sn40Pb solder alloy. The contact angle was measured as a function of flux, surface preparation procedures, and solder temperature. Our testing led to the following conclusions:

1. Using the Diversey 9-333 surface etch treatment, we found that the fluxes B1452, A260HF, B2508, A250HF, and A611 resulted in contact angles of $29° \pm 5°$, $45° \pm 6°$, $53° \pm 5°$, $53° \pm 11°$, and $61° \pm 11°$, respectively, when diluted 1:1 by volume with isopropyl alcohol.

2. Changing the Kovar surface treatment to an electropolish in a solution of acetic and perchloric acids significantly improved the contact angles with the use of A611 ($31° \pm 2°$) and A260HF ($37° \pm 2°$).
3. More so than the actual surface condition of the Kovar, the solder-flux interfacial tension, $\gamma_{LF}$, played a significant role in the solderability of this system.

   Altering the degree of dilution of the B1452 flux changed the contact angle predominantly through differences in the values of $\gamma_{LF}$.

   The by-products generated by the flux-substrate chemical interaction appeared to influence $\gamma_{LF}$, and subsequently the contact angle. Therefore, the surface condition of the Kovar substrate left after cleaning affected solderability more through $\gamma_{LF}$ than through the condition of the Kovar, per se.
4. With the use of A611 and B1452, solder temperatures in the range 215°C to 288°C caused an overall drop in the contact angle from $34° \pm 2°$ to $27° \pm 4°$ with B1452, and an insignificant change for A611 as determined by a linear-least-squares analysis. In both cases, the behaviors of $\theta_c$ were not monotonic.
5. Optical microscopy of the solder film surfaces demonstrated appearances that were very dependent on the flux in use as well as the Kovar surface condition.
6. Scanning electron microscopy of cross-sectional views of the Kovar-solder film interface showed no evidence of cracking and an absence of large-scale intermetallic formation (to within the resolution of the x-ray maps) between the tin component of the solder and the nickel, cobalt, and iron constituents of the Kovar.
7. T-peel strength measurements were made of Diversey-cleaned Kovar-OFHC joints bonded with 60Sn40Pb solder in which the Kovar was coated with one of the five fluxes, and the copper with A611. Only a rudimentary correlation was found between the solderability contact angle and the T- peel strength of each respective flux. A qualitative evaluation of the sample fracture surfaces did reveal that the fluxes affected the Kovar-solder bond strength irrespective of extrinsic properties such as void formation.

# References


[1]L. Murr, *Interfacial Phenomena in Metals and Alloys* (Reading, PA; Addison Wesley, 1975).

[2]L. Wilhemy, *Ann Phys 119: 177 (1863).*

[3]A. Mayhew and G. Wicks, "Solderability and Contact Angle," *Proc Inter NEPCON* (1971), p. 45.

[4]A. Mayhew and K. Monger, "Solderability by Meniscometry," *Proc Inter NEPCON* (1972), p. 53.

[5]*Metals Handbook, Ninth Ed* (Metals Park, OH: ASM 1985) Vol. 9, p. 52.

[6] P. Jacquet, "Electrolytic and Chemical Polishing," *Metall Rev 1* (1956), p. 169.

[7] H. Manko, *Solders and Soldering*, (New York; McGraw-Hill 1979), p. 227.

[8] E. Westerlaken, "Rosin Solder Flux Residues Shape Solvent Cleaning Requirements," *Elec Pack and Prod* (February 1985), p. 118.

[9] D. Lovering, "Rosin Acids React to Form Tan Residues," *Elec Pack and Prod*, (February 1985), p. 232.

[10]W. Archer, "Analysis of Rosin Flux Residue After Soldering and Cleaning," *Elec Pack and Prod*, (February 1985), p. 152.

[11]J. Jellison, D. Johnson, and F. Hosking, "Statistical Interpretation of Meniscograph Solderability Results," *IEEE Trans on Parts, Hybrids, and Pack, PHP-11* (1976), p. 126.

[12] I. Okamoto, T. Takemoto, M. Miautani, and I. Mori, "Physical Meaning of Wetting Curve Traced by Meniscograph Wettability Tester (Report II)," *Trans Jap Weld Res Inst 14* (1985), p. 1.

[13]J. Shipley, "Influence of Flux, Substrate, and Solder Composition on Solder Wetting," *Weld Res Suppl* (Oct 1975, p. 357-s.

[14]M. Schwartz, *Brazing* (Metals Park, OH: ASM Inter 1987), p. 10.

[15]E. Brothers, "Intermetallic Compound Formation in Soft Solders," *The Western Electric Engineer* (Spring/Summer 1981), p. 49.

[16]A. Latin, "The Influence of Fluxes on the Spreading Power of Tin Solders on Copper," *Trans Faraday Soc 34* (1930), p. 1384.

[17] F. Howie and E. Hondros, "The Surface Tension of Sn-Pb Alloys in Contact With Fluxes," *J. Mater Sci 17* (1982) p. 1432.

[18]J. Bickerman, *Surface Chemistry for Industrial Research* (New York: Academic Press, 1949), pp.65-85.

[19]D. White, "The Surface Tension of Liquid Metals and Alloys," *Metall Rev 13* (1968), p. 73.

[20]A. Schwaneke, W. Folde, and V. Miller, "Surface Tension and Density of Liquid Tin-Lead Solder Alloys," *J. Chem and Eng Data 23* (1978), p. 298.

[21]W. Wallace, SNL Report#087079, Div 1823 (Albuquerque, NM: Sandia National Laboratories, August 27, 1987).

# APPENDIX

# Expression for the Meniscus Cross-Sectional Area

A derivation of the expression describing the cross-sectional area of the meniscus, Eq. (6) in the introduction, is given below. Equation (3) describes the value of any point on the meniscus as a function of the vertical elevation, y, of that point above the solder level and is reproduced below:

$$1 - \sin\theta = \frac{g\rho y^2}{2\,\gamma_{LF}} \,. \tag{A-1}$$

As indicated in Mayhew, et al.,[4] Eq (A-1) can be expressed in terms of the Cartesian coordinates as diagrammed in Figure 3, in which x is the dependent variable:

$$x = \sqrt{\frac{2\gamma_{LF}}{\rho g}}\left[\frac{1}{2\sqrt{2}}\ln\frac{\sqrt{2+q}}{\sqrt{2-q}} - \frac{1}{2\sqrt{2}}\ln\frac{\sqrt{2+q_c}}{\sqrt{2-q_c}} - q + q_c\right] \tag{A-2}$$

where

$$q = \sqrt{2 - \frac{\rho g y^2}{2\gamma_{LF}}}$$

and

$$q_c = \sqrt{2 - \frac{\rho g H^2}{2\gamma_{LF}}} \,.$$

All other parameters are as defined earlier. Equation (A-2) differs from that in Reference 5 in that $\rho$ has replaced the expression, $(\rho - \rho_o)$. The derivation of the meniscus cross-sectional area, A, by the authors will begin from this point. Rearranging the expressions for q and $q_c$ by dividing each side by $\sqrt{2}$ and defining k as:

$$k = \frac{\rho g}{4\gamma_{LF}} \,, \tag{A-3}$$

the following expression will be integrated:

$$x = \sqrt{\frac{2\gamma_{LF}}{\rho g}}\left[\frac{1}{2\sqrt{2}}\ln\left(\frac{1+\sqrt{1-ky^2}}{1-\sqrt{1-ky^2}}\right) - \frac{1}{2\sqrt{2}}\ln\left(\frac{1+\sqrt{1-kH^2}}{1-\sqrt{1-kH^2}}\right)\right. \tag{A-4}$$

$$\left. + \sqrt{2}\sqrt{1-ky^2} - \sqrt{2}\sqrt{1-kH^2}\right]$$

The cross-sectional area of the meniscus is determined by the integration of Eq (A-4) term-by-term over the interval, $0<y<H$:

$$A = \int_0^H x(y)\,dy \,. \tag{A-5}$$

Integration of the first term is initiated by the substitution of u for $(1\text{-}ky^2)^{1/2}$ so that the expression becomes (omitting the coefficients):

$$\int_o^H \ln\left[\frac{1+\sqrt{1-ky^2}}{1-\sqrt{1-ky^2}}\right]dy = \frac{-1}{\sqrt{k}}\int_1^{\sqrt{1-kH^2}} \ln\left(\frac{1+u}{1-u}\right)\frac{u}{\sqrt{1-u^2}}\,du \ . \qquad \text{(A-6)}$$

Next, integration-by-parts was performed on the right-hand side of equation (A-6), in which:

$$v = \ln\left(\frac{1+u}{1-u}\right) \qquad dv = \frac{2}{(1-u^2)}\,du$$

$$w = -\sqrt{1-u^2} \qquad dw = \frac{u}{\sqrt{1-u^2}}\,du \ . \qquad \text{(A-7)}$$

The resulting expression for the integral in Eq (A-6) is:

$$H\ln\left[\frac{1+\sqrt{1-kH^2}}{1-\sqrt{1-kH^2}}\right] - \frac{2}{\sqrt{k}}\sin^{-1}(1-kH^2)^{1/2} + \frac{\pi}{\sqrt{k}} \ . \qquad \text{(A-8)}$$

Integration of the other three terms on the right-hand side of Eq (A-4) is easily performed or located in the appropriate tables so that the expression for the area, A, becomes:

$$A = \frac{H}{2}\sqrt{\frac{4\gamma_{LF}}{\rho g} - H^2} \ . \qquad \text{(A-9)}$$